Build the Synthesis-Property Relationship of Tough Sonogels with EPR and Mechanical Study

by

Yixun Cheng

Department of Mechanical Engineering

McGill University, Montreal, Quebec, Canada

August 2024

A thesis submitted to McGill University in partial fulfillment of the requirements for the degree of Master of Engineering.

Table of Contents

Abstract

Conventional tough hydrogel preparation is usually based on thermal or photochemistry. In comparison, other forms of energy received much less attention. Here, we formulated the paradigm of ultrasound in the preparation of double-network tough sonogels with the classic polyacrylamide-alginate system as an example. Compared with heat and light, ultrasound has a much higher energy-release rate, deep penetration depth, and supports multimode adjustment. High-speed and polarized imaging were employed to monitor the dynamic process of gelation transformation. The underlying sonochemical mechanism was revealed with the EPR study for the first time. It turned out that glycerol plays dual functions as a benign initiator and viscosity modifier in sonogel synthesis, among which its chemical role is far more determinative. To further build the synthesis-property relationship of sonogels, we studied the effect of ultrasound intensity and monomer-to-crosslinker ratios. As sonochemical reactions and mechanical disruption co-exist during sonication, the above factors are not separate but intrinsically coupled and co-determine the net effect on sonogels, including whether to form a gel or toughen a gel. The highest toughness of PAAm-alginate sonogels recorded here was over 600 J m^{-2}. Mechanical and structural characterization demonstrated the overall better performance of sonogels over thermal or photo-initiated gels, including a much faster gelation modality, higher toughness, and more uniform and porous microstructure. This research is dedicated to providing a fundamental perspective on the application of mechano- or sonochemistry in hydrogel preparation and relevant soft matter engineering.

Résumé

La préparation conventionnelle d'hydrogels résistants est généralement basée sur la thermochimie ou la photochimie. En comparaison, d'autres formes d'énergie ont reçu beaucoup moins d'attention. Ici, nous avons formulé le paradigme des ultrasons dans la préparation de sonogels résistants à double réseau en prenant comme exemple le système classique polyacrylamide-alginate. L'imagerie à haute vitesse et l'imagerie polarisée ont été utilisées pour surveiller le processus dynamique de transformation de la gélification. Le mécanisme sonochimique sous-jacent a été révélé pour la première fois par l'étude RPE. Il s'est avéré que le glycérol joue un double rôle en tant qu'initiateur bénin et modificateur de viscosité dans la synthèse des sonogels, parmi lesquels son rôle chimique est bien plus déterminant. Pour approfondir la relation synthèse-propriétés des sonogels, nous avons étudié l'effet de l'intensité des ultrasons et des rapports monomère/réticulant. Comme les réactions sonochimiques et les perturbations mécaniques coexistent pendant la sonication, les facteurs susmentionnés ne sont pas séparés mais intrinsèquement couplés et codéterminent l'effet net sur les sonogels, y compris la formation d'un gel ou le durcissement d'un gel. La ténacité la plus élevée des sonogels PAAm-alginate enregistrée ici était supérieure à 600 J m-2. La caractérisation mécanique et structurelle a démontré la meilleure performance globale des sonogels par rapport aux gels thermiques ou photo-initiés, y compris une modalité de gélification beaucoup plus rapide, une ténacité plus élevée et une microstructure plus uniforme et poreuse. Cette recherche vise à fournir une perspective fondamentale sur l'application de la mécano-chimie ou de la sonochimie dans la préparation des hydrogels et l'ingénierie de la matière molle.

Acknowledgments

I would like to express my gratitude first to my supervisor, Prof. Jianyu Li. Thank you for your continuing instruction in my academic research. I'm amazed by how you always propose some novel ideas to push the study more interestingly and attractively and also hope this innovative thinking can be integrated into my future research. Moreover, thank you for your warm encouragement when I got frustrated sometimes by obstacles in the research and your strong support for my choice of further career development. "I think chemists are creative." This is not just trust in my capability but gives me confidence and motivation to try to find solutions to daily questions.

Secondly, I would like to acknowledge my research fellows and all of our lab members, especially Louis Jacques-Bourdages who helped me a lot either in building experiment platforms or in analyzing and interpreting results. Without his generous help, it would never be possible to turn our ideas into reality. I appreciate acquainting and interacting with everyone in daily life. The laughter and happiness that occurred in the office, lab, or outdoor activities would become my treasured memory.

Last but not least, I would like to send my sincere and greatest thanks to my parents. It is their continuous nourishment and dedication that shaped me who I am today. Thank you for your strongest support in enabling me to keep chasing my dreams in academia. I've always felt grateful and fulfilled for everything you gave me.

Contribution of Authors

Yixun Cheng and Jianyu Li conceived and designed the study. Yixun Cheng planned and conducted all the experiments. Louis Jacques-Bourdages helped build the high-speed and polarized imaging platform. All authors participated in the analysis of the results. Yixun Cheng wrote the manuscript. Jianyu Li supervised the project.

List of Figures and Tables

List of Abbreviations

Abbreviation	Definition
AAc	acrylic acid
AAm	acrylamide
Alg	alginate
APS	ammonium peroxide disulfate
ATRP	atom transfer radical polymerization
α-CD	α-cyclodextrin
Chi	chitosan
DFT	density functional theory
DLP	digital light processing
DMPO	5,5-Dimethyl-1-pyrroline *N*-oxide
DN	double network
EPR	electron paramagnetic resonance
FTIR	Fourier-transform infrared
Gly	glycerol
GO	graphene oxide
HEMA	poly(2-hydroxyethyl methacrylate)
HIFU	high-intensity focused ultrasound
LCST	lower critical solution temperature
MBAA	*N*, *N*-methylene bisacrylamide
NHS	*N*-hydroxysuccinimide ester
NIPAM	*N*-isopropylacrylamide
PAAc	poly(acrylic acid)
PAAm	poly(acrylamide)
PAMPS	poly(2-acrylamido-2-methyl propane sulfonic acid)
PAN	polyacrylonitrile
PEGDA	poly(ethylene glycol) diacrylate
PEG	poly(ethylene glycol)
PET	polyethylene terephthalate
PNIPAM	poly(*N*-isopropylacrylamide)

PVA	poly(vinyl alcohol)
RAFT	reversible addition-fragmentation chain-transfer
SAXS	small-angle X-ray scattering
SEM	scanning electron microscope
SLA	stereolithography
TA	tough adhesive
TEMED	*N*,*N*,*N*,*N*-Tetramethylethylenediamine
US	ultrasound
WAXS	wide-angle X-ray scattering

Chapter 1. Introduction

1.1. Background

Hydrogels are a class of soft materials consisting of hydrophilic polymer networks that can swell but not dissolve in aqueous solvents. Either in chemical composition or mechanical properties, hydrogels show a great resemblance to biological tissues and thus are considered one of the most promising substitutes for biomaterials. They have been developed in a variety of biomedical and biomimetic applications so far, including bioadhesives, soft robotics, biosensors, as well as biotherapeutic carriers. To endow hydrogels with specific properties or functions, a series of preparation methodologies are well-established, which could be summarized into two categories according to the energy types of the driving force, including thermal synthesis and photochemistry. Within the existence of corresponding initiators, heat or light can initiate the polymerization of monomers or crosslink of preexisting long chains to construct swollen polymer networks. Peroxides, ketones, and azo compounds are commonly used as thermal or photo-initiators in the traditional batch synthesis of hydrogels. Generally, the required conditions for gelation transformation are mild with a long curing time. For example, the preparation of classic double-network poly(acrylamide) (PAAm)-alginate hydrogels needs to be placed in molds overnight. Moreover, residual chemical initiators may constitute a potential risk factor if the as-prepared hydrogels are in situ formed for biological applications or directly used in vivo.

In comparison, ultrasound (US) is an alternative accessible, compatible, and eco-friendly energy source but receives much less attention, particularly in the realm of hydrogel preparation as well as soft matter engineering. The frequency of most ultrasound used in chemical synthesis (or sonochemistry) varies from 20kHz and 10MHz. Distinct from thermal synthesis or

photochemistry, ultrasound has a much higher energy release rate through the process of acoustic cavitation. Nucleated bubbles can grow over periodic compression and rarefaction cycles and finally collapse (for the inertial cavitation) in liquids to generate mechanochemically reactive hot spots. Both theoretical simulation and preliminary experimental data showed that inside the imploded cavities are transient and localized extreme conditions, which could reach a center temperature of ~ 5000 K and high pressure of ~ 1000 atm. The unusual condition enables the homolytic cleavage of molecules and thereby generation of free radicals (primary sonochemistry occurring in the gas phase). These reactive species may diffuse into solvents and further get involved in secondary sonochemical reactions, such as coupling, addition, and polymerization reactions. For example, monomers can propagate into long chains under ultrasonic irradiation. The strong shear forces accompanied by bubble collapse, on the other hand, tend to create mechanical disruptions and play a destructive role in the media. Taking advantage of ultrasound-activated mechano- or sonochemistry, chain growth or chain scission of polymers could get oriented and selective control, depending on material systems, sonication parameters, liquid media, etc.

Although ultrasound-assisted polymerization has developed a relatively systematic methodology, either in free-radical or controlled polymerization, it's been rarely reported in hydrogel synthesis. Representative examples include the study of Ulanski et.al. on poly(ethylene glycol) diacrylate (PEGDA) family hydrogels and Cass et.al. on poly(2-hydroxyethyl methacrylate) (HEMA) hydrogels. Besides, Yang et.al. reported hydrogel formation by ultrasound-triggered thiol-norbornene crosslink. In their research, the reaction progress and chemical properties of sono-synthesized hydrogels (or sonogels) were mainly characterized. However, given the substantial difference between ultrasound and other preparation methodologies, there still exists a significant knowledge vacancy in the synthesis-property relationship of sonogels. The impact of strong disturbance induced by acoustic

cavitation on the process of gelation transition has yet to be investigated. Moreover, no direct clear evidence has been explored before to corroborate mechanisms of sonochemical gelation, which are essential to deepen our understanding of the chemical essence of sonogel synthesis and accommodate their further use in advanced fabrication such as direct sound printing and spatially controlled adhesion reported recently.

Therefore, in this thesis, we formulated paradigms for using ultrasound to prepare tough hydrogels for the first time and dug into the sonochemical mechanisms with electron paramagnetic resonance (EPR) study. We chose (poly)acrylamide and alginate as a model material system to construct double-network tough sonogels under 20kHz non-focused US irradiation. Acrylamide monomers would polymerize and crosslink into a network during sonication. Real-time imaging with high-speed or polarized cameras showed that strong cavitation and accompanying liquid streaming fostered precursors get cured into a complete piece of gel within just several minutes. EPR spectra and reaction progress profiles validated the dual function of glycerol additives and offered a profound view of reaction mechanisms. Glycerol increases the systemic viscosity that moderates the diffusion rate of reactive radical species and extends their working lifetime while, more crucially, it serves as an essential source of benign initiators to launch gelation. We further benchmarked the synthesis-property relationships by studying the effects of US intensity (I) and monomer-to-crosslinker ratio (φ_m). Together with the glycerol ratio, they co-determine the gelation profile of sonogels, which applies to diverse material systems and helps customize the properties of sonogels. The toughest sonogel recorded could reach a fracture energy of over 600 J m^{-2}. Compared with hydrogels initiated by thermal or photo-chemistry, sonogels have much faster gelation kinetics, more uniform and porous microstructure, and better toughness performance.

1.2. Thesis structure

This thesis includes five chapters as follows. A brief introduction to the research objectives and a thesis structure are included in the first Chapter. Chapter 2 provides a comprehensive literature review, covering broader backgrounds of tough hydrogels and sonochemistry. Specifically, the design strategies, synthetic methods, and application examples of tough hydrogels will be mentioned revolving around the first topic, while the established classic sonochemistry theory, synthetic applications, as well as rising sono-technologies in soft materials, will be discussed in the second part. Chapter 3 presents the experimental section of the project, including materials and methodologies. Chapter 4 expands discussions of the results, specifically including the preparation of sonogels, the EPR study for mechanisms of sonochemical gelation, and the synthesis-property relationships of sonogels. The conclusion and outlook will be provided in Chapter 5 to summarize key findings, significance, as well as possible future work relevant to this project.

Chapter 2. Literature Review

2.1. Tough Hydrogels

Consisting of mostly water, conventional hydrogels are generally soft and fragile. To adapt them to various application scenarios, many strategies have been developed to improve their mechanical behaviors, among which toughness is a primary demand, enabling hydrogels with robustness to resist deformation and maintain elasticity. In recent years, toughening strategies and relevant experiment methods have been well established. In the following, the section reviews tough hydrogels systematically from their design and preparation to applications.

2.1.1 Design Principles

The toughness of hydrogels is characterized by fracture energy (Γ) that can be divided into the intrinsic fracture energy of the hydrogel (Γ_0) and the fracture energy due to mechanical dissipation in the region around the crack (Γ_D)(I). Γ_0 is the energy required to break polymer

$$\Gamma = \Gamma_0 + \Gamma_D \tag{1}$$

chains per unit area on the crack plane, which is determined by the product of energy required to rupture a single chain and the number of chains across the unit area. It's estimated that the intrinsic fracture energy of hydrogels is no more than 10 J m^{-2}. In comparison, the contribution from mechanical dissipation can be designed tactically to far exceed 10^2 or 10^3 J m^{-2}. Depending on the specific dissipation zones, a high Γ_D usually requires hydrogels can sustain high levels of stress and strain with large stress-strain hysteresis (in the process zone) or accommodate high traction and large crack opening (in the bridging zone). Thus, the general design principles for tough hydrogels can be summarized into two aspects, to improve energy dissipation upon crack propagation and maintain a high stretchability or elasticity after deformation.

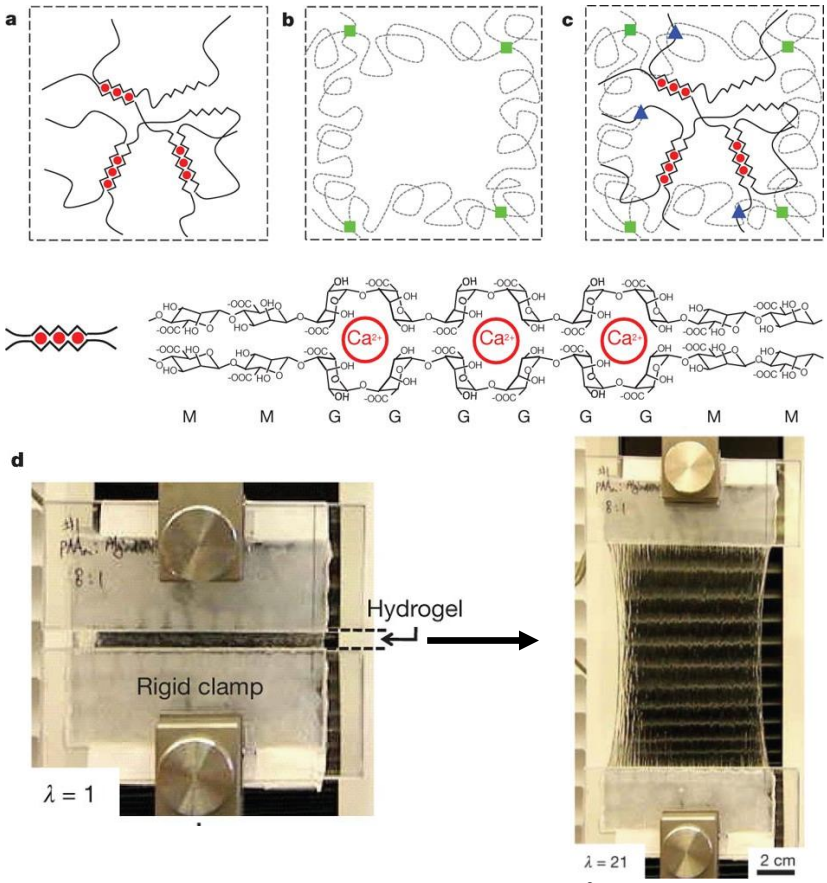

Figure 2.1 Schematics of **(a)** ionic crosslinks through Ca^{2+} in the alginate gel, **(b)** covalent crosslinks through N, N-methylene bisacrylamide (MBAA), and **(c)** two intertwined polymer networks by covalent crosslinks between amine groups on polyacrylamide chains and carboxyl groups on alginate chains in the hybrid gel. **(d)** The hybrid gel was stretched to 21 times its initial length in a tensile machine without rupture. (Reproduced from (*2*), Copyright 2012, Spring Nature)

Double-network hydrogels

To enhance the energy dissipation of hydrogels, Gong et.al. utilized the fracture of polymer chains and pioneered introducing a second network to the traditional hydrogels, also known as the double-network (DN) tough hydrogel. (*3-5*) Among the two interpenetrating networks, the first network usually consists of densely crosslinked synthetic polymers, while the second network performs higher flexibility due to loosely crosslinked long chains. Upon large deformation, the mechanical energy stored in the brittle polymer chain gets dissipated by the

fracture of covalent bonds, while the stretchable second network maintains the overall elasticity of hydrogel and allows it to return to the original configuration after the external force is released. Quantities of research have shown the wide applicability of this strategy, and some classic examples include polyacrylamide (PAAm)-poly(2-acrylamido-2-methyl propane sulfonic acid) (PAMPS) hydrogel (*4*), polyacrylic acid (PAAc) (*6*) and agarose (*7*) hydrogel, poly(vinyl alcohol) (PVA)-chitosan hydrogel, etc. In 2012, Suo et.al. developed a highly stretchable and tough hydrogel of PAAm and alginate ('tough gel' below). (*2*) Different from dual covalently crosslinked networks, alginate is ionically crosslinked by calcium ions. The hybrid gel could be stretched over twenty times without rupture and showed maximum fracture energy of 8700 J m^{-2}. During deformation, the progressive unzipping of G blocks in alginate dissipates substantial energy without causing localized damage to either alginate or PAAm chains, so the gel performed pronounced hysteresis and negligible deformation after unloading. The synergy mechanisms of crack bridging and background hysteresis offered guidance to the design of diverse hybrid tough hydrogels.

Reversibly crosslinked tough hydrogels

Another strategy to induce mechanical dissipation depends on the reversible or physical crosslinking of polymer chains, including ligand-receptor interaction, hydrogen bonds, hydrophobic interaction, electrostatic interaction (*8*), cation-pi interactions (*9*), etc. For example, Gong et.al. from Hokkaido University developed polyampholytes-based physical hydrogels that exhibited great toughness and viscoelasticity. (*10*) Depending on the distribution of strength through inter- or intrachain complexation, the electrostatic attraction between cationic and anionic monomers could formulate strong bonds or weak bonds that serve as permanent and sacrificial crosslinks, respectively. The strong crosslinks maintain the shape of hydrogel under deformation while the rupture of weak bonds dissipates mechanical energy to enhance the fracture resistance. Distinguished from the Ca^{2+}-crosslinked alginate network

mentioned before, this supramolecular hydrogel shows a complete self-recovery with no sliding of chains under large deformation. The background hysteresis in a single loading-unloading process involves a two-stage recovery process and illustrates an obvious time dependence, indicating the competition between the elasticity of the intact primary chain and the strength of temporarily reformed bonds. Moreover, the hysteresis loops overlapped perfectly under cyclic tests, and this high fatigue resistance was attributed to a high density of weak but dynamically reversible bonds that ensured fast self-healing and shock absorbance by generating high internal friction. A balance between strong bonds and weak bonds is required to achieve a tough physical hydrogel. This polyampholyte strategy is universal to various ionic pairs and they all demonstrated a high gel strength, toughness, and viscoelasticity regardless of the modulus change.

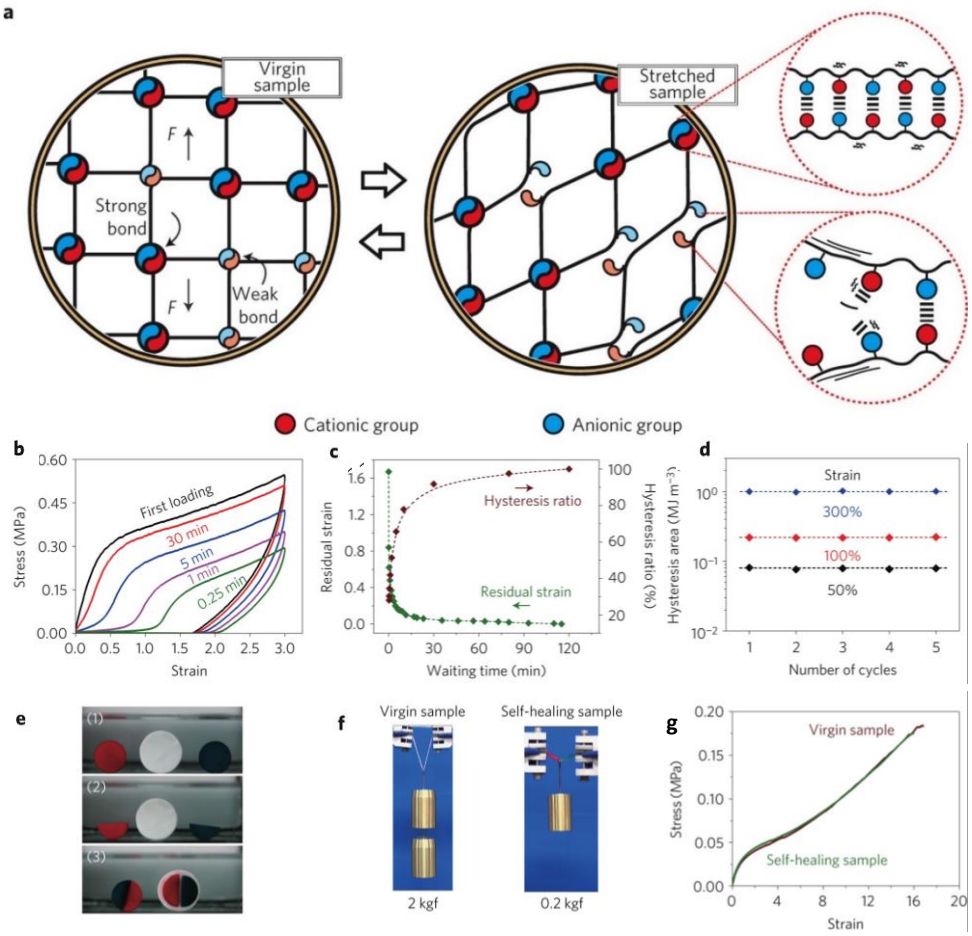

Figure 2.2 (a) Illustration of polyampholyte networks with ionic bonds of different strengths (strong bonds and weak bonds). **(b-d)** Self-recovery and background hysteresis of

polyampholyte supramolecular gels. **(e-f)** Demonstration of self healing and adhesion between two cut samples as well as load bearing tests. **(g)** stress-strain curves of the original and self-healed samples, showing a high fatigue resistance. (Reproduced from (*10*), Copyright 2013, Spring Nature)

Fiber-reinforced tough hydrogels

Besides, the incorporation of fibers or fillers can also toughen hydrogels by significantly increasing the energy dissipation in the bridging zone during crack propagation. Commonly used fibers include woven poly(ε-caprolactone) fiber scaffolds, polyacrylonitrile (PAN), cellulose, and silk nanofiber composites. For instance, Suo and Vlassak et.al. fabricated a stainless-steel fiber-reinforced PAAm-alginate hybrid gel. Results of tensile tests showed that the random fiber network could dissipate much energy by frictional sliding before being ripped apart, leading to a combined effect of stiffening, strengthening, and toughening the hydrogel matrix and enabling it to attain large deformation. (*11*)

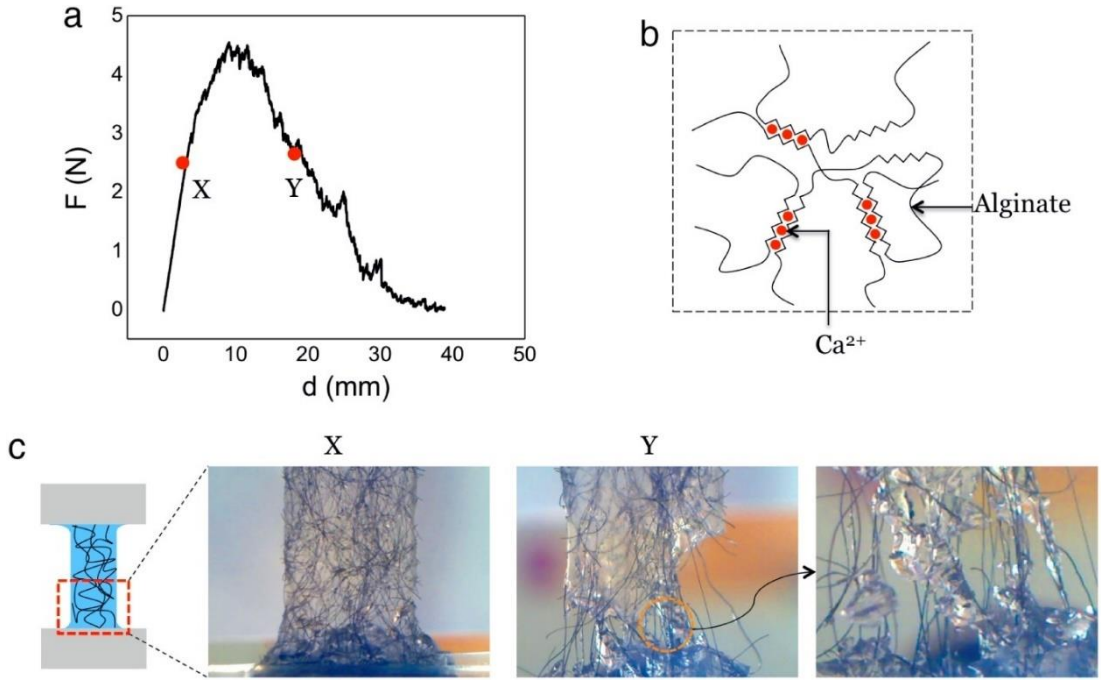

Figure 2.3 Failure mechanism of a brittle and weak alginate hydrogel composite. **(a)** The force-displacement curve from a tensile test. **(b)** Schematic of the structure of alginate hydrogels. **(c)** Images at two stages during the tensile test (point X at small deformations, point Y at large deformations). (Reproduced from (*11*), Copyright 2014, Elsevier)

Mechanoresponsive self-strengthening hydrogels

Similar to the living tissues that can autonomously renew and adapt to mechanical surroundings, recent studies reported that hydrogels could also mimic this self-strengthening behavior to maintain a high toughness.

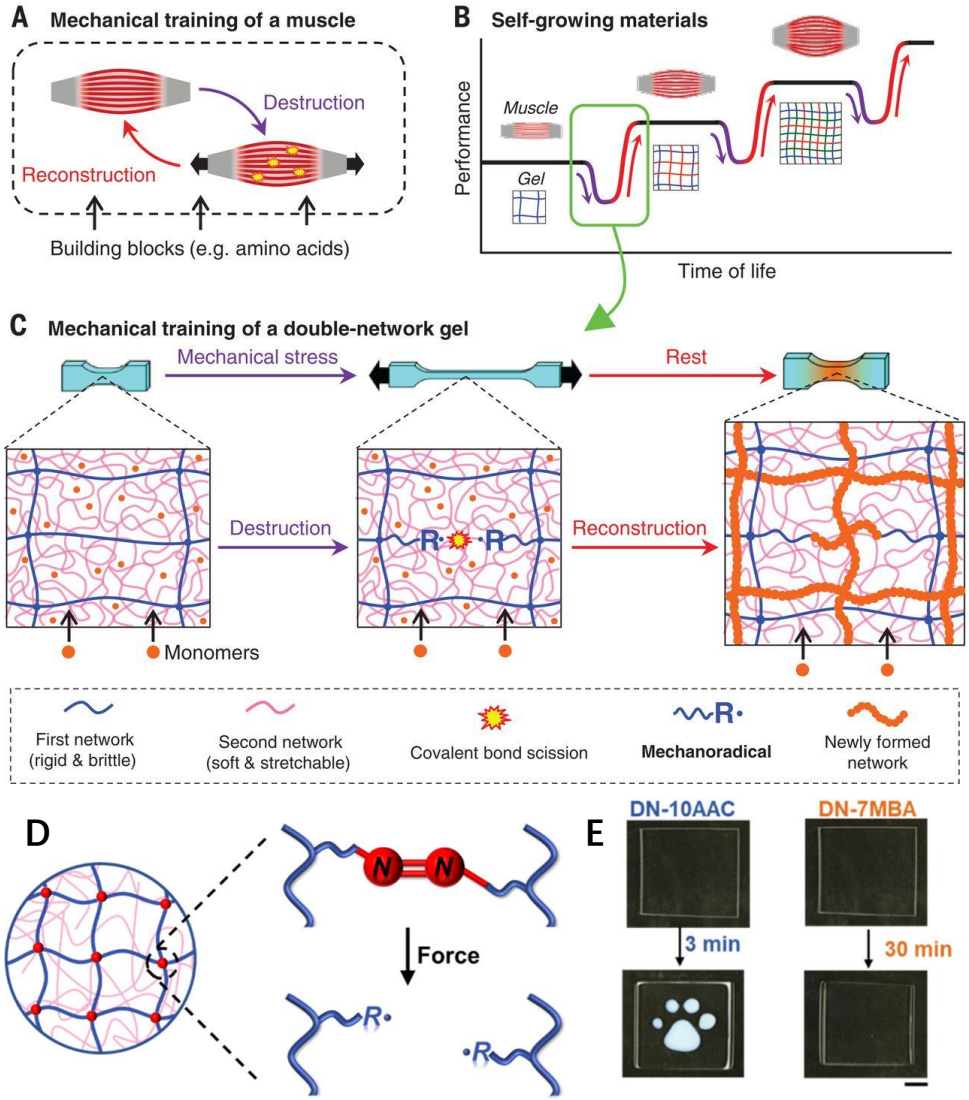

Figure 2.4 Conceptual schematic of the self-growth materials induced by mechanoradicals. **(A)** Repeated mechanical training and nutrient supply makes muscle stronger and bigger. **(B)** Both tissues and gels get weakened initially but then recover even show enhanced performance due to mechanical stimuli. **(C)** The strategy to develop self-growing materials based on mechanical training of DN gels. Mechanical stress leads to the breakage of the brittle network, whereas the highly stretchable network maintains the integrity of the gel. **(D)** Schematic of the breakage of azo crosslinkers to generate stable mechanoradicals. (Reproduced from (*12*), Copyright 2019, AAAS) **(E)** Illustration of DN gels fed with monomer NIPAM with azo or MBAA crosslinkers.

(Reproduced from (*13*), Copyright 2022, ACS)

In 2019, Gong et.al. innovated a self-growing tough hydrogel induced by mechanoradicals. (*12*)They constructed an original PAMPS-PAAm tough hydrogel, among which polymer strands in the brittle PAMPS network would rupture and generate mechanoradicals without causing bulk failure of gels. With a sustained monomer supply, these mechanoradicals triggered the formation of a new network and realized self-growth in strength and size. Cyclic tests validated the persistent growth of DN gels during repetitive stretching, showing potential applications in space-selective lettering. For the success of constructing self-growing hydrogels, a key challenge is to create a sufficient concentration of mechanoradicals. In contrast to traditional MBAA crosslinkers, the cleavage of azoalkane crosslinkers requires lower yield stress but creates mechanoradicals of five-fold concentration, which was validated by density functional theory (DFT) simulation and practical mechanical tests. (*13*) The joint incorporation of traditional and azoalkane crosslinkers into the DN gels exhibits an exceptional radical generation performance.

Apart from energy dissipation, maintaining elasticity and stretchability is another class of toughening approach. As the stretch limit of polymer chains is proportional to the square root of the number of monomers ($\lambda_{lim} \propto \sqrt{n}$), long chains with a higher molecular weight tend to be incorporated into the hydrogel to accommodate larger stretching, such as PVA and poly(ethylene glycol) (PEG). (*14*) In addition, ideal elastic networks (*15*) or equivalent multifunctional crosslinkers also facilitate the construction of tough hydrogels.

Multifunctional crosslinker hydrogel

As shown in previous examples, either physical or chemical crosslinker used in conventional hydrogels generally has a low functionality, suggesting that once the bridging polymer chain ruptures, the connections between crosslinkers are no longer effective, which easily leads to the fracture of hydrogels. However, micro- or nanodomains can connect to multiple polymer chains and help control crosslinking densities and inter-crosslinking distances. Although some short chains may fracture upon deformation, there are remaining intact segments to facilitate load redistribution and prevent crack propagation. (*1, 16*) It's worth mentioning that these multifunctional crosslinking agents can be separately added (such as silicate nanoplatelets, clay nanoparticles, and macromolecular microspheres) or spontaneously formed by existing polymer chains (represented by the crystalline region in PVA networks).

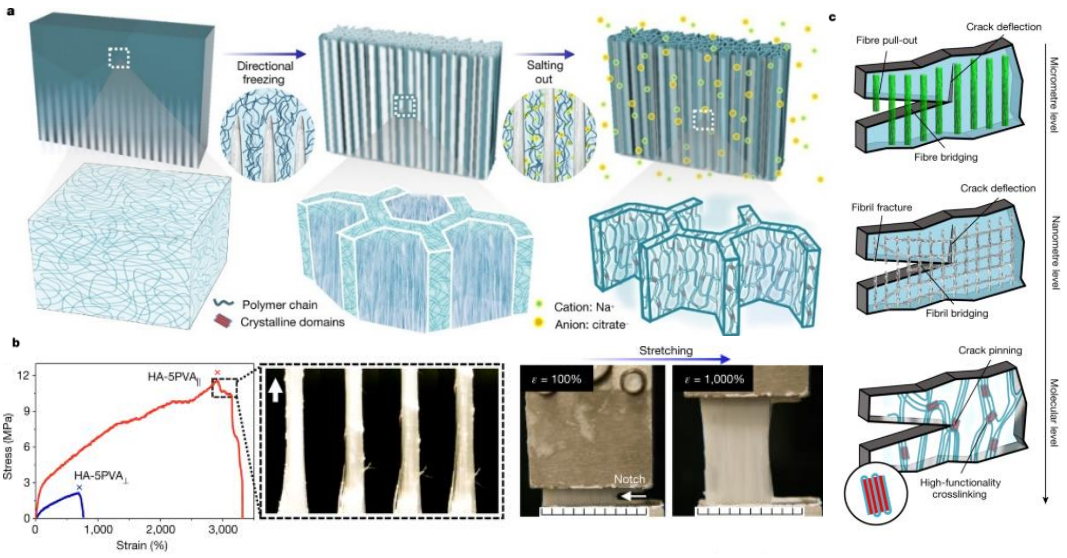

Figure 2.5 (a) Freezing-assisted salting-out fabrication procedure of the HA-PVA hydrogels. Structural formation and polymer chain concentration, assembly and aggregation during the freezing-assisted salting-out fabrication process. **(b)** Tensile stress–strain curve of HA-5PVA hydrogel in the parallel (∥) and perpendicular (⊥) directions relative to the alignment direction. (Left) Images of tensile loading with a pre-crack in the parallel direction. (Right) **(c)** Toughening mechanisms at each length scale. (Reproduced from (*17*), Copyright 2021, Spring Nature)

Slide-ring tough hydrogel

In 2001, Okumura and Ito tactically designed a polyrotaxane hydrogel with slide-ring topology. (*18*) They utilized α-cyclodextrin (α-CD) as mobile crosslinking agents on monodisperse PEG chains to equalize tension and release stress among adjacent chain segments during deformation. As the sliding α-CD acts as a pulley, they conceptualize the mechanism model as the 'pulley effect'. Compared with hydrogels toughened by energy-dissipative structures, there is no rupture of sacrificial bonds in this topological slide ring gel so it can achieve damageless reinforcement of toughness and perform high fatigue resistance under cyclic loading-unloading tests. (*19-21*) Recently, the Ito group further explained the toughening mechanism of PEG-based slide-ring gels by WAXS and SAXS study. (*22*) It turned out that the stretched slide-ring gels showed diffraction spots in WAXS and sharp streaks in the SAXS pattern, indicating the formation of crystalline precursors between PEG chains. They proposed that strain-induced crystallization was the origin of the high mechanical reversibility of the slide ring gels. By controlling the PEG volume fraction and the coverage rate of α-CDs, it's straightforward to formulate designated slide-ring gels.

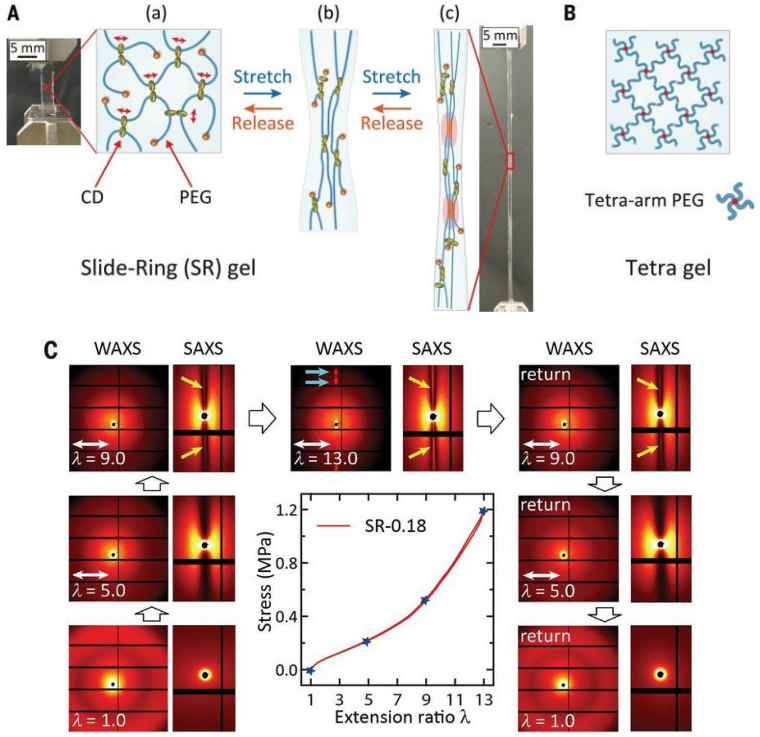

Figure 2.6 Schematic of **(A)** slide-ring gel with movable cross-links composed of CDs. The close-packed structure of PEG is formed and destroyed during stretching and releasing. **(B)**

tetra gel with fixed cross-links. **(C)** WAXS and SAXS patterns of slide-ring gels to observe the structural transition under cyclic loading. (Reproduced from (*22*), Copyright 2021, AAAS)

Highly entangled tough hydrogel

Although the slide ring strategy is effective in constructing tough hydrogels, such gels are not resistant to swelling in water due to a comparatively low crosslinking density. Practically, or hydrogels fabricated from preexisting polymers like PVA or PEG, crosslinks endow them with swelling resistance but can also lead to low stiffness and toughness.

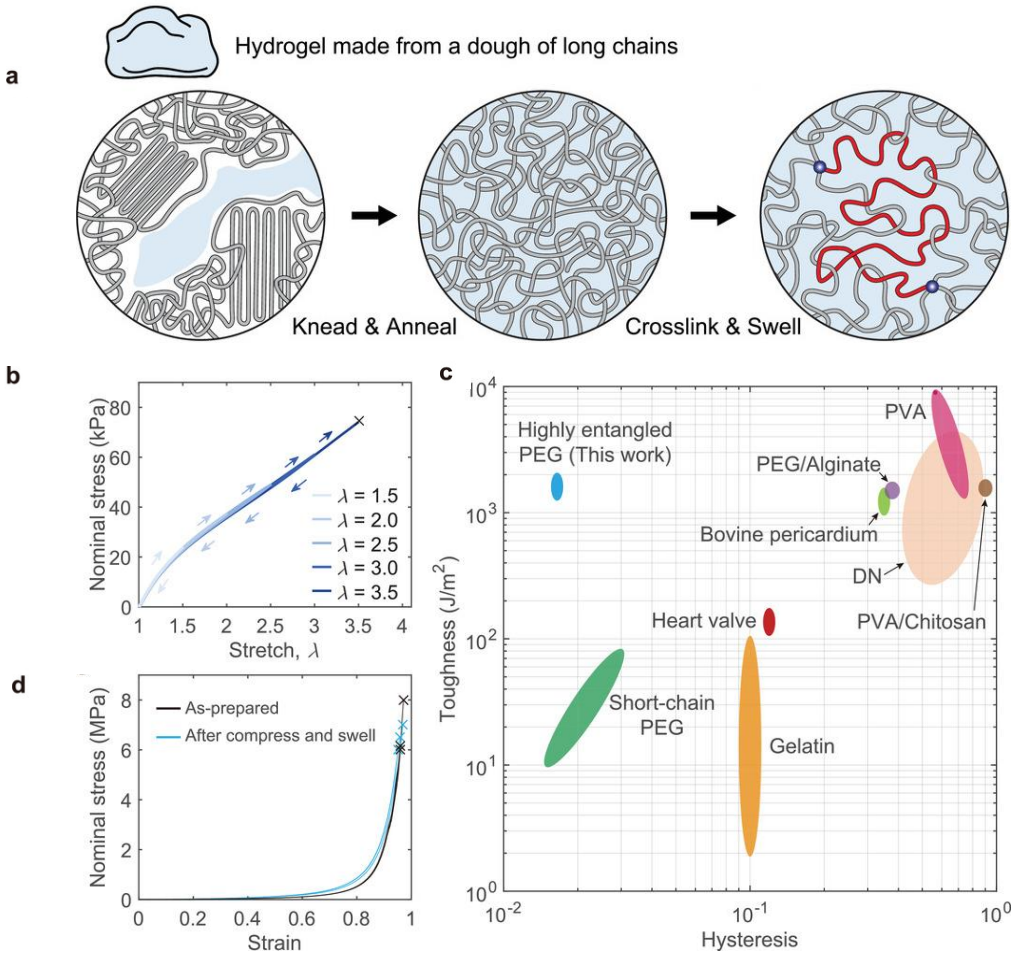

Figure 2.7 (a) Make a hydrogel from a dough of long polymers: mix long polymers with a small amount of water, knead and anneal the mixture to form a homogenized dough, crosslink the polymers into a network, and swell the network in water to equilibrium. **(b)** A highly entangled PEG hydrogel exhibits near-perfect elasticity with negligible hysteresis. **(c)** Highly entangled PEG hydrogels are compared with existing hydrogels on the toughness-hysteresis plane. (d) The nominal stress-strain curves of highly entangled hydrogel during two compression tests. (Reproduced from (*23*), Copyright 2022, Wiley-VCH)

To solve this conflict, Suo et.al. reported a new strategy using entanglements of long polymer chains to offset the negative effects induced by a low amount of crosslinkers but also provide enough stiffness and toughness even swelling in water. (*23*) Inspired by doughs, they fabricated the highly entangled tough gel from PEG of an ultrahigh molecular weight (8×10^6 g mol^{-1}). By cyclic kneading and annealing, entanglements in the topological network greatly outnumber crosslinks. The dense entanglements can partially serve as crosslinkers to constrain the swelling but not embrittle the polymer network. On the other hand, scarce covalent crosslinkers allow redistribution of tension along the long chain and thus endow the gel with excellent toughness. Results from tensile tests validated a low friction coefficient, high fatigue threshold, and low hysteresis, further supporting the theory of slips of entanglements to equalize tension during stretching.

2.1.2 Preparation Methods

Although the design strategies of tough hydrogels may vary greatly from each other, their preparation methods are relatively unified. According to the driving force of initiation, they can be summarized into two categories, thermal synthesis or photochemistry. As the chemical essence of tough hydrogels is swollen polymer networks, thermal- or photoinitiators are usually added in the precursors to launch the polymerization of monomers or crosslinking between existing polymer chains. Common initiators include peroxides, ketones, and azo compounds. For example, ammonium peroxide disulfate (APS) acted as the thermal initiator in the free-radical polymerization of small-molecule vinyl monomers like acrylamide and acrylic acid. With the help of N,N,N,N-Tetramethylethylenediamine (TEMED) accelerators (*24, 25*), the curing of PAAm-alginate tough hydrogel can be completed overnight at room temperature. For another, ketone compounds like benzophenone and α-ketoglutaric acid can cleave into ketyl radicals and carbonyl radicals in the presence of another hydrogen donor and under UV light irradiation, where the latter usually leads to the polymerization of monomers. (*26, 27*)

Compared with thermal initiation, the photoinitiation process is considered more efficient and flexible, allowing less concerns of residual initiators and on-demand control of initiation spots. These versatility and advantages are genuinely crucial in advanced manufacturing or patterning of hydrogels. For instance, vat photopolymerization has been applied in hydrogel printing, including stereolithography (SLA) and digital light processing (DLP). (*28, 29*) To obtain a better control of resolution, the polymerization kinetics of materials and the pixel size or motion mode of light exposure are essential considerations. The maturing spatial patterning allows for customized design of hydrogels in artificial organs, tissue models, soft robots, etc.

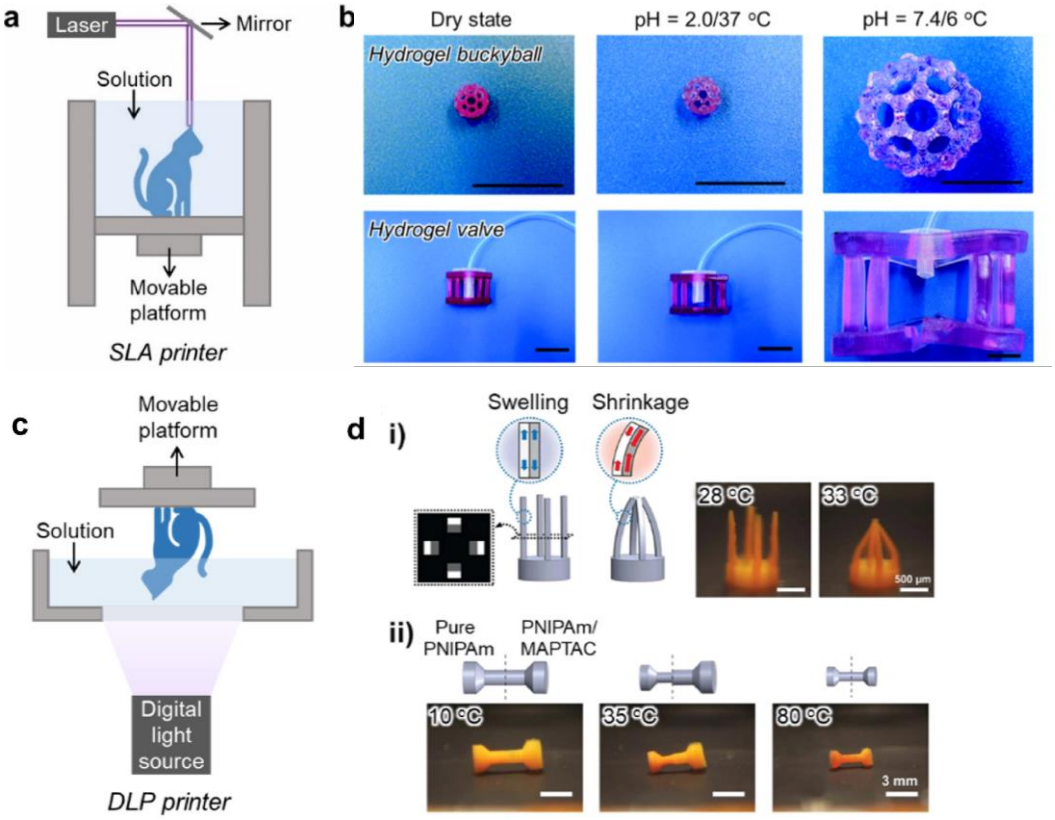

Figure 2.8 (a) Schematic of SLA 3D printer. (Copyright 2020, Elsevier) **(b)** SLA printed stimuli responsive DN hydrogels in a buckyball or valve shape at various pH conditions. (*30*) (Reproduced from (*30*), Copyright 2017, RSC) **(c)** Schematic of DLP 3D printer. (Reproduced from **(d)** DLP printed PNIPAM microstructures and their programmed temperature dependent deformation. (*31*) (Reproduced from (*31*), Copyright 2018, Spring Nature)

2.1.3 Applications

The intriguing properties of tough hydrogels (such as resilience, strength, sustainability, biocompatibility, etc.) enable them to be promising candidates in a series of biomedical or biomimetic applications. In the following, a detailed introduction will be expanded on tough bioadhesives, tissue engineering, as well as soft robotics sequentially. (*16, 32*)

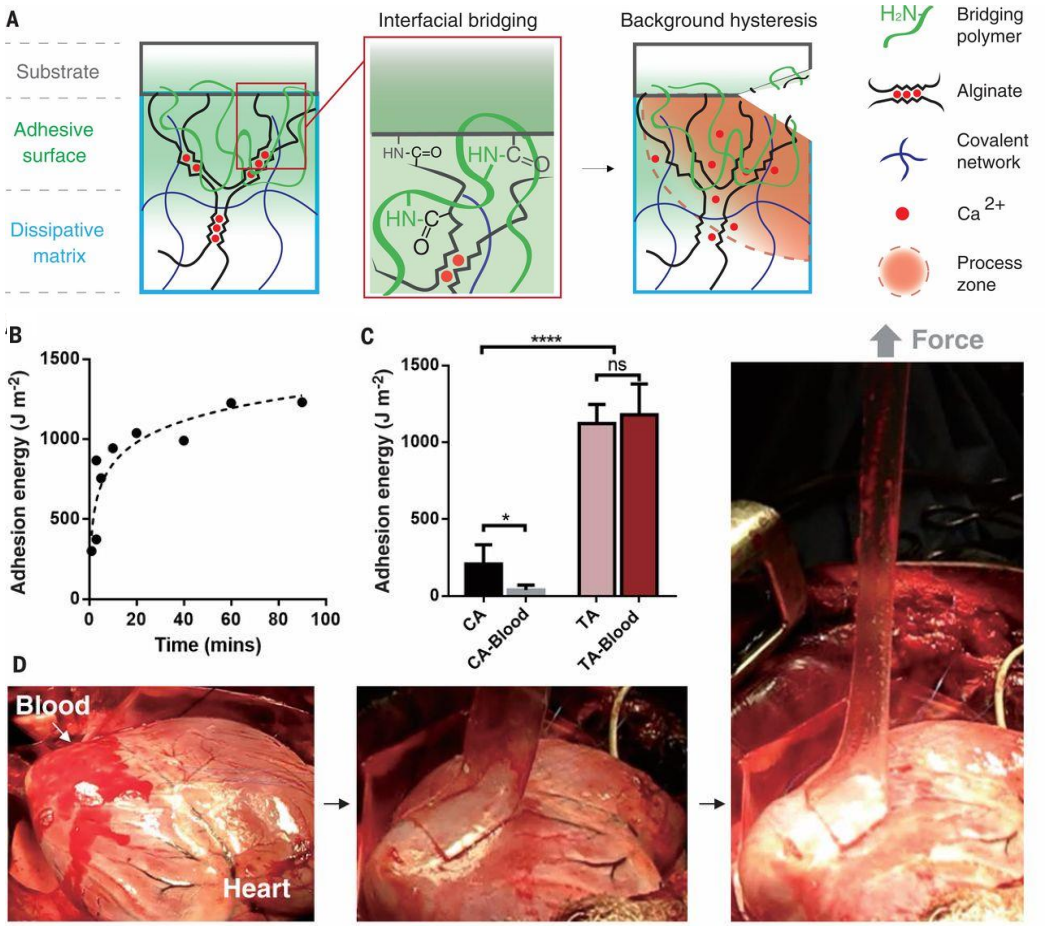

Figure 2.9 (A) Schematic of design of tough adhesives, which consist of a dissipative matrix and an adhesive surface. **(B)** Adhesion kinetics of TAs to porcine skin. **(C)** Comparison of TAs versus commercial adhesives placed on porcine skin with and without exposure to blood. **(D)** Images of in-vivo test on a beating porcine heart with blood exposure. (Reproduced from (*33*), Copyright 2017, AAAS)

Tough bioadhesives

As an emerging healthcare technology, bioadhesives are promising alternatives to conventional tissue attachment techniques that can be used in diverse applications such as drug delivery,

wound dressing, and hemostasis. (*34*) Compared with existing commercial fibrin and cyanoacrylate glue, new-generation bioadhesives based on tough hydrogels demonstrated better performance, including exceptional strength or toughness, good adaptability, and controlled or prolonged adhesion. In 2017, Li et.al. developed the very first tough bioadhesives (TAs) applicable to various wet surfaces and reached maximum adhesion energy of around 1000 J m^{-2}. (*33*) The TAs consisted of two layers, interpenetrating bridging polymers as the adhesive surface and tough hydrogels as the dissipative matrix. The adhesive surface can covalently bond to or physically interact with tissues to achieve bioadhesion, while the hydrogel patch dissipates much energy effectively to ensure high toughness. The TAs demonstrated wide applications either as a sealant for wound closure in a porcine heart or a hemostatic dressing in a hepatic hemorrhage model.

Subsequently, the theoretical framework of hydrogel (bio-)adhesion was established by Suo et.al. (*35*) and Li et.al. (*36*) and further applied in the follow-up research. The key principle is to build strong connections at the hydrogel-tissue interface while ensuring large mechanical dissipation of the hydrogel matrix. According to the difference in interactions, bioadhesion can be divided into physical adhesion (secondary interactions like van der Waals, hydrogen bonds, electrostatic forces, etc.), chemical adhesion (covalent bonds, ionic bonds, etc.), topological adhesion, or a synergized strategy. For example, Yuk et.al. developed a dry double-sided tape that can form instant dependable adhesion with wet tissues. (*37*) The novel tape combined biodegradable biopolymers like chitosan with a crosslinked PAAc network grafted by N-hydroxysuccinimide ester (NHS). When attached to wet tissue surfaces, the hygroscopic PAAc network starts to swell and form physical connections at the interface, including hydrogen bonds and electrostatic interactions. Within minutes, the covalent crosslinking between NHS and primary amine groups further strengthens the toughness, which could reach over 1000 J m^{-2} of adhesion energy as measured. Inspired by these dry tapes, Zhao and colleagues designed

another tough bioadhesive based on interpenetrating networks of PVA and PAAc-NHS. (*38*) This patch not only supports instant adhesion capability through hybrid crosslinking but can be triggered by sodium bicarbonate and glutathione solution to detach from and reposition tissues in a benign manner. In 2021, Deng et.al. introduced graphene oxide (GO) into the above PVA-PAAc-NHS networks and fabricated an electrical bioadhesive interface. (*39*) The microstructure of PVA-GO composites constrained the in-plain swelling of adhesives when in contact with wet tissues, and thereby abstained potential geometric mismatch, distortion, and delamination of the electrical interface from bioelectronic devices.

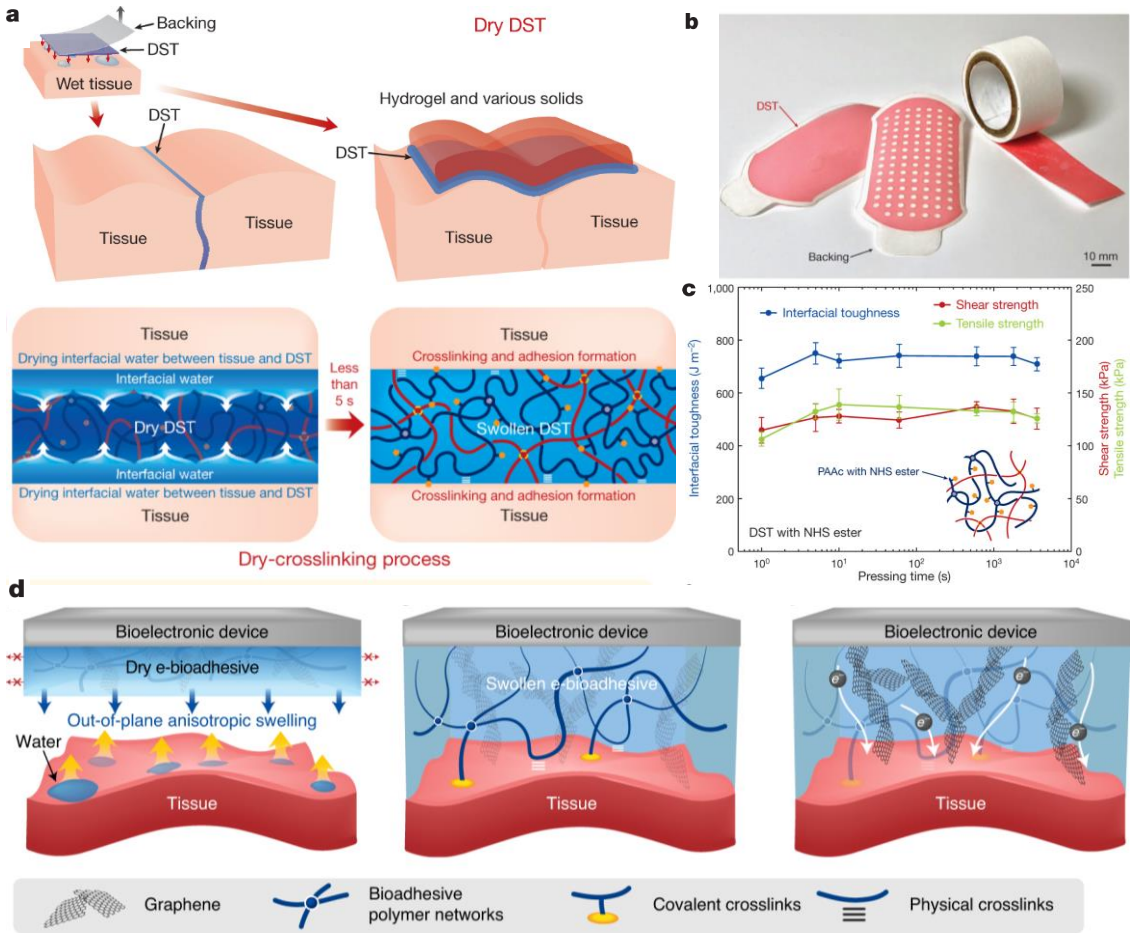

Figure 2.10 (a) Schematic of the working mechanism of double-sided tapes as tough adhesives, including temporary dry crosslinking by hydration and swelling of the tape, as well as covalent crosslinking by forming amide bonds. **(b)** The double-sided tapes can take on various shapes due to high flexibility in fabrication. **(c)** Interfacial toughness and shear and tensile strength versus pressing time for wet porcine skins adhered using the DST with NHS ester. (Reproduced

from (*37*), Copyright 2019, Spring Nature) **(d)** Materials design and properties of the graphene nanocomposite-based e-bioadhesive interface capable of providing anisotropic out-of-plane swelling. (Reproduced from (*39*), Copyright 2021, Spring Nature)

Tissue engineering

The material and structural diversity endow tough hydrogels with functional flexibility and tunability, which is advantageous in serving as biomaterials for tissue engineering. For instance, a synthetic DN tough hydrogel of poly(N,N-dimethyl acrylamide)-PAMPS has been developed as an acellular cartilage scaffold for cartilage regeneration. (*40*) The gel exhibited a comparable compression modulus and friction coefficient to cartilage. Zhang et.al. from Harvard formulated a tough double-network bioink for microfluidic bioprinting. The bioink consists of hybrid crosslinked networks of gelatin and alginate, illustrating an excellent toughness of 616.3 J m^{-2}, good biocompatibility, and a shear-thinning behavior with a rising temperature. (*41*) The bioprinted arterial conduits demonstrate physiological vasoconstriction and vasodilatation responses, showcasing their potential for in vitro disease studies and as in vivo grafts for vascular surgeries. Besides, tough hydrogels can also serve as extracellular matrix that allows embedded stem cells or other primary cells to grow and differentiate into functional tissues. Substantial research has established that the mechanical elasticity of hydrogels affects mechanotransduction of cells and thus fundamental cellular processes, offering guidelines for oriented tissue engineering. For example, Luo et.al. reported a vertical 3D extrusion cryo-bioprinting technology and fabricated cell-laden hydrogel constructs with a high-aspect-ratio and diverse patterning. (*42*) The gelatin methacryloyl (GelMA) bioink shows an anisotropic mechanical property via directional freezing, which is crucial to successful construction of the muscle-tendon unit.

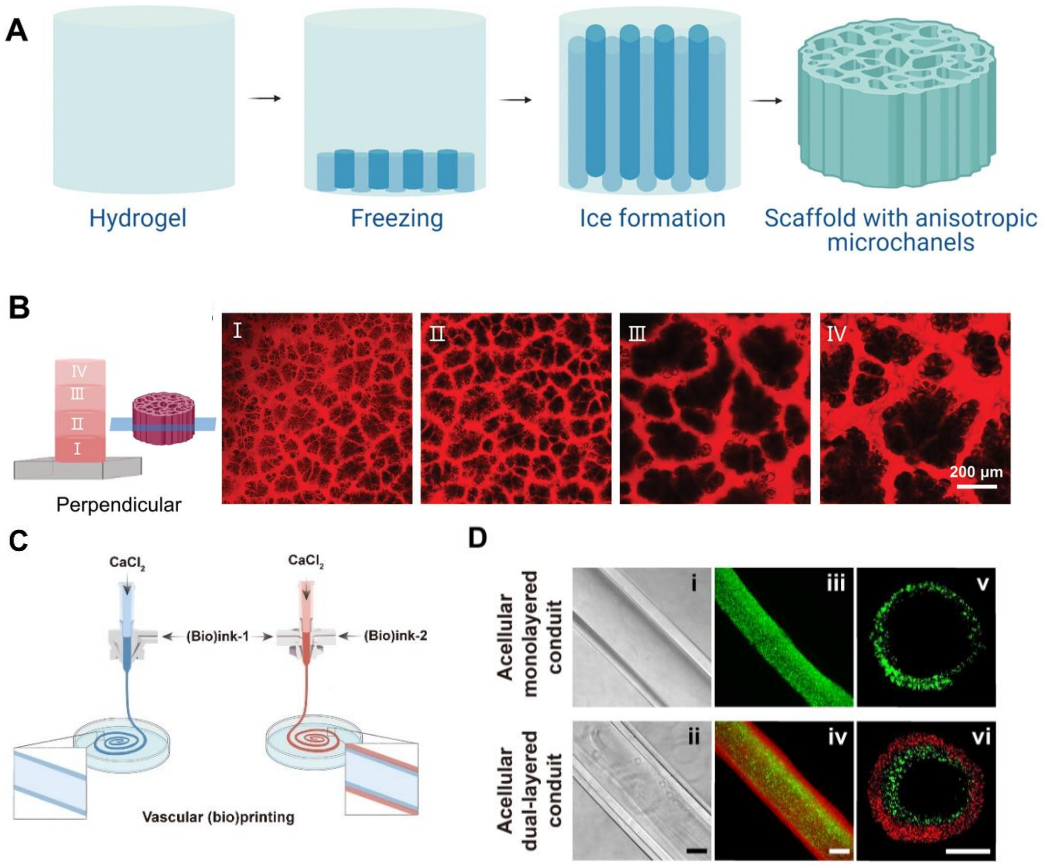

Figure 2.11 (A) Schematic showing the GelMA-based hydrogel forms interconnected gradient and anisotropic microchannels along the vertical axis during vertical 3D cryo-bioprinting. **(B)** Fluorescence microscopy images showing the effect of temperature gradient on the microchannel sizes in the GelMA construct, where microchannels are perpendicular to the freezing direction. (Reproduced from (*42*), Copyright 2022, Wiley-VCH) **(C)** Schematics of microfluidic extrusion (bio)printing of monolayered and dual-layered vascular conduits with gelatin-alginate DN tough hydrogels. **(D)** Representative lateral-view bright-field images and fluorescence microscopic images of monolayered (top) and dual-layered (bottom) hollow tubes. (Reproduced from (*41*), Copyright 2022, AAAS)

Soft robots

The stimuli-responsiveness of hydrogels make them engaging candidates for soft actuators. Distinct from rigid metal counterparts, the flexible and compliant actuators are particularly preferred in biomedical fields. (*43, 44*) A representative example is poly(N-isopropylacrylamide) (PNIPAM) hydrogel, which can occur volume phase transition across the

lower critical solution temperature (LCST). However, single-network PNIPAM hydrogel is typically brittle and fragile. Chen et.al. synthesized a hybrid PNIPAM-algiante tough hydrogel and prototyped the all-hydrogel bilayer beam and the four-arm gripper. (*45*) Instead of using calcium ions, they immersed the DN gel in aluminum chloride ($AlCl_3$) solution, where the role of Al^{3+} were twofold, crosslinking the alginate network and tuning the LCST of hydrogel. The toughened hydrogel exhibited a higher Young's modulus, stretchability (~ 2.5 times), yield stress (6.3 ± 0.3 MPa), and superior energy dissipation (1610 ± 30.9 kJ/m^3). By varying the concentration of $AlCl_3$, the resulting gel can perform differing thermoresponsive properties. This discriminated performance allows fabrication of an intelligent bilayer soft actuator, whose bending angle and speed can be controlled by tuning the temperature.

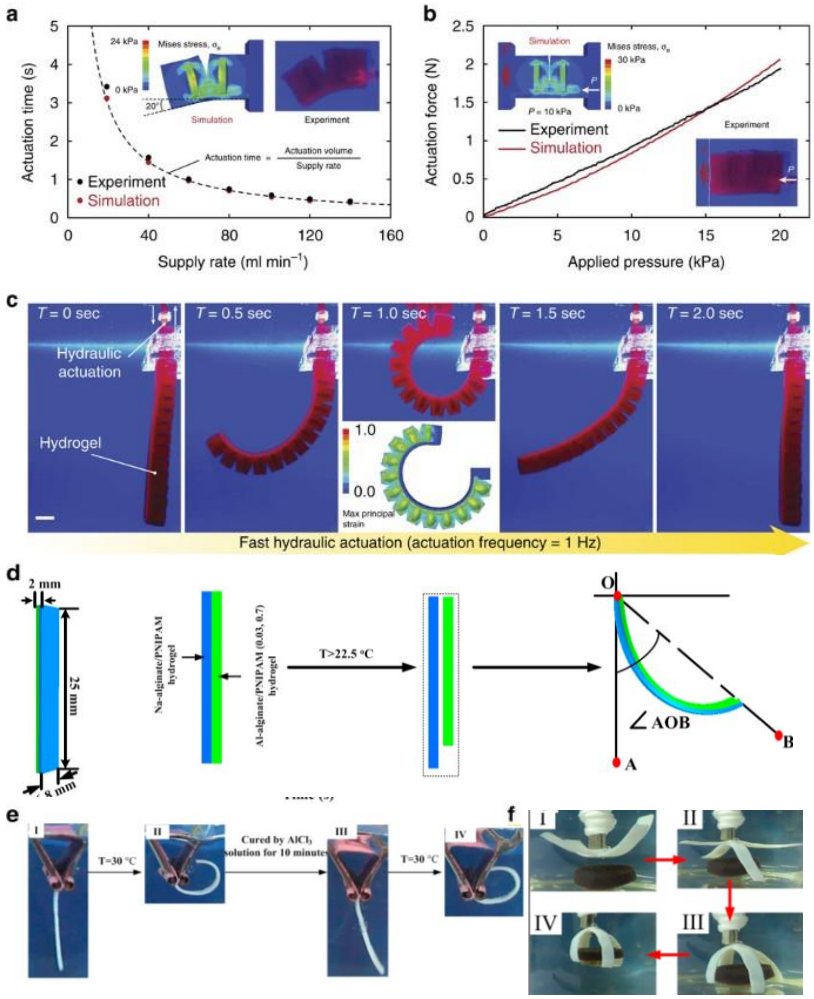

Figure 2.12 (a-b) The performance of hydraulic hydrogel actuators. **(a)** Actuation time versus supply rate **(b)** Actuation force versus applied pressure in both experiments and finite element

simulations. **(c)** Fast bending actuation of the hydraulic hydrogel actuator with actuation frequency around 1 Hz. (Reproduced from (*46*), Copyright 2017, Spring Nature) **(d)** Schematic of a bilayer beam actuator made of Al-alginate and PNIPAM and the definition of bending angle. **(e)** Images of the gripping process of the four-arm gripper captured a black hydrogel disc. (Reproduced from (*45*), Copyright 2015, ACS)

Wang and colleagues designed hydraulic hydrogel actuators using PAAm-alginate hydrogels. (*46*) Due to a high optical and sonic transparency, this actuator could achieve natural camouflage in water, allowing high-fidelity imaging and controlled actuation, which supports their further application in biomimetic or biomedical settings like sustained release of bioactive components.

2.2. Ultrasound and Sonochemistry

This section reviews the mechanochemical effects of ultrasound and fundamental principles of sonochemistry. The classic sonochemistry theory pioneered by K. Suslick et.al. will be expanded in the first section. (*47*) Subsequently, we will illustrate instances showcasing the diverse applications of ultrasound in the synthesis, degradation, or other mechanochemistry of polymers. Although ultrasound-assisted polymerization has developed a considerably systematic methodology, either in free-radical or controlled polymerization, it's been rarely reported in the preparation of hydrogels and advanced manufacturing of soft materials. Thus, the last section of this chapter will look back to previous studies on sonogel synthesis and the very recent progress in direct sound printing as well as ultrasound-mediated controlled bioadhesion.

2.2.1 Sonochemistry Fundamentals

Ultrasound technology has been extensively used in medical diagnosis and therapy, such as bioimaging (*48*), thermal ablation, drug delivery (*49*), and histotripsy. High-frequency acoustic waves can provide valuable visual insights into tissues or create localized sonothermal effects

at the lesion area. In comparison, lower-frequency ultrasound received much less attention in terms of industrial and commercial uses. Since the 1980s, the theoretical framework of classic sonochemistry has been laid out gradually by K. Suslick et.al. from the University of Illinois at Urbana-Champaign, subsequently advancing the utilization of ultrasound in chemical synthesis and the evolution of mechanochemistry. (*50, 51*) Different from traditional energy sources like heat or light, ultrasound (particularly in the low-frequency range of below 1 MHz) has an extremely high energy release rate through the process of nonlinear acoustic cavitation, which includes three phases, nucleation, growth, and implosive collapse of bubbles. Specifically, as the sound waves are periodically vibrating, the formation of cavities occurs when the negative peak pressure overcomes the liquid's tensile strength. Nucleated bubbles start growing during the oscillating expansion and compression cycles, and can reach a critical size eventually where they resonate with sound waves and enable the most efficient energy absorption. In inertial cavitation, such cavities would overgrow until no longer attain themselves, when the surrounding liquid rushes in and the cavities implode.

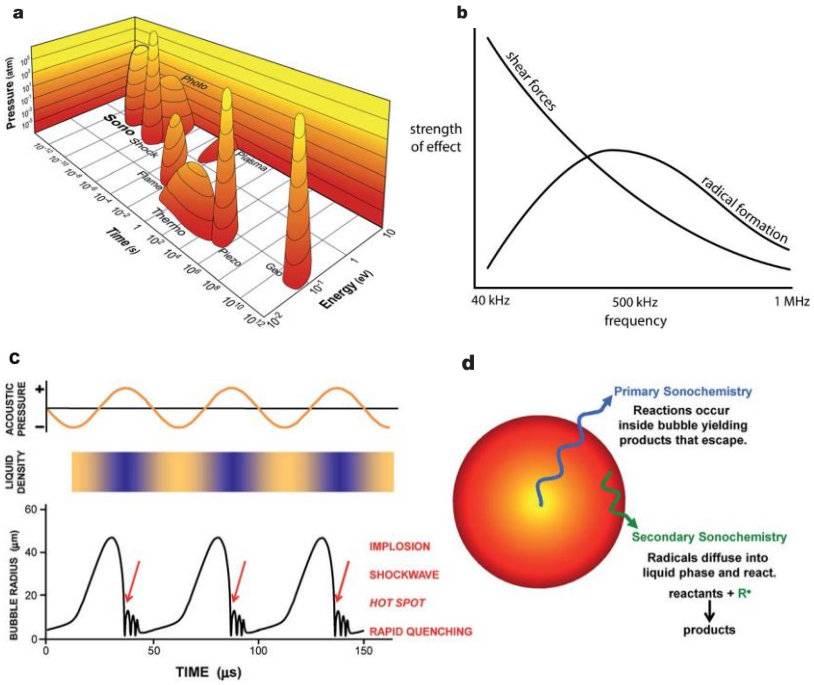

Figure 2.13 (a) Islands of chemistry as a function of time, pressure, and energy. Sonochemistry occupies a unique short-time, high-energy, and high-pressure space.(*51*) (Copyright 2014, RSC)

(b) Generalized profiles for the "strength" of each of these effects at a given operating ultrasonic frequency.(*52*) (Copyright 2019, Wiley-VCH) **(c)** Schematic illustration of the process of acoustic cavitation: the formation, growth, and implosive collapse of bubbles in a liquid irradiated with high-intensity ultrasound. (*51*) (Copyright 2014, RSC)

As the energy stored in the bubble gets released within a very short time, a transient extreme condition is created locally to form hot spots with an estimated high temperature of ~ 5000 K and a high pressure of ~ 1000 bar. (*53-55*) These intense conditions yield homogenous sonochemistry, represented as the homolytic cleavage of small molecules (from either solvent or reactant) and thereby the production of reactive free radicals. These chemical species further diffuse into the liquid phase and launch secondary sonochemical reactions, like polymerization, addition, or condensation reactions. (*56*)

The profile of sonochemistry can be tailored with multiple factors such as acoustic frequency (*57*), acoustic intensity, ambient temperature, static pressure, and the nature of liquid media. A representative parameter is the cavitation threshold, the minimum acoustic intensity only above which sonochemical reactions could occur. As the nucleation of cavities involves competition between the negative acoustic pressure and the cohesive forces of a liquid, factors working on each side will affect the threshold value. For example, the presence of gas molecules introduces weak spots to lower the liquid's tensile strength and therefore requires less energy to induce cavitation. On the other hand, increasing the viscosity improves the cohesive force acting in the liquid, making it harder for the negative pressure in the rarefaction cycle to overcome that value and further create bubbles. The applied frequency is another crucial factor. For sound waves with higher frequencies, it becomes more difficult to achieve the available time to form cavities. More energy is lost to the molecular motion of the liquid. It's estimated that compared with the low-frequency band ($< 10^4$ Hz), the demand for ultrasonic power to initiate cavitation experiences a more pronounced increase, particularly in the higher band of above 10^5 Hz.

Furthermore, the influence of temperature on sonochemical reactions diverges from typical chemical systems. While the Arrhenius equation posits a positive correlation between reaction rate and ambient temperature, sonochemical environments exhibit an inverse relationship. In such settings, elevated systemic temperatures elevate vapor pressure, creating additional cushioning for bubble implosion, consequently reducing the central temperature and resulting in a decline in the reaction rate.

In addition to creating reactive chemistry, the strong mechanical effects accompanied by acoustic cavitation also have profound effects on liquid media. As the bubble collapses result in an inrush of liquid filling the cavity, intense shear forces are produced. In a homogenous medium, polymer strands in the high-gradient shear field close to the bubble tend to move faster than those segments further away, leading to the elongation and finally scission of chains. This ultrasound-induced chain scission shows an apparent chain-length dependence, where polymers with a higher molecular weight tend to scission more rapidly at the same acoustic intensity. Similar to primary sonochemistry occurring inside the cavities, the cleavage of polymer chains is still dominated by homolytic rupture enabling the production of mechanoradicals. By tailoring the acoustic intensity, solvent properties, initial molecular weight, or chemical structure of polymers, ultrasound-activated polymer mechanochemistry could be designed in a controlled and predictable modality. (*58*) Especially for reactions proceeding through radicals, sonication could be an effective method to change their reaction pathway or progress.

For a heterogenous medium, cavitation bubbles get deformed when created at a phase interface. The following liquid jets propagate across the bubble toward the interface at a high velocity and induce emulsion (for the liquid-liquid interface) or corrosion (for the solid-liquid interface). For example, sonicated emulsions generally have a smaller size than usual, favoring enhancing the efficacy of phase transfer-catalyzed reactions. The powerful impact of agitation would also

leave disorganized surfaces, dislocations, vacancies, or local defects on solid particles, bringing potential opportunities for ionic reactions.

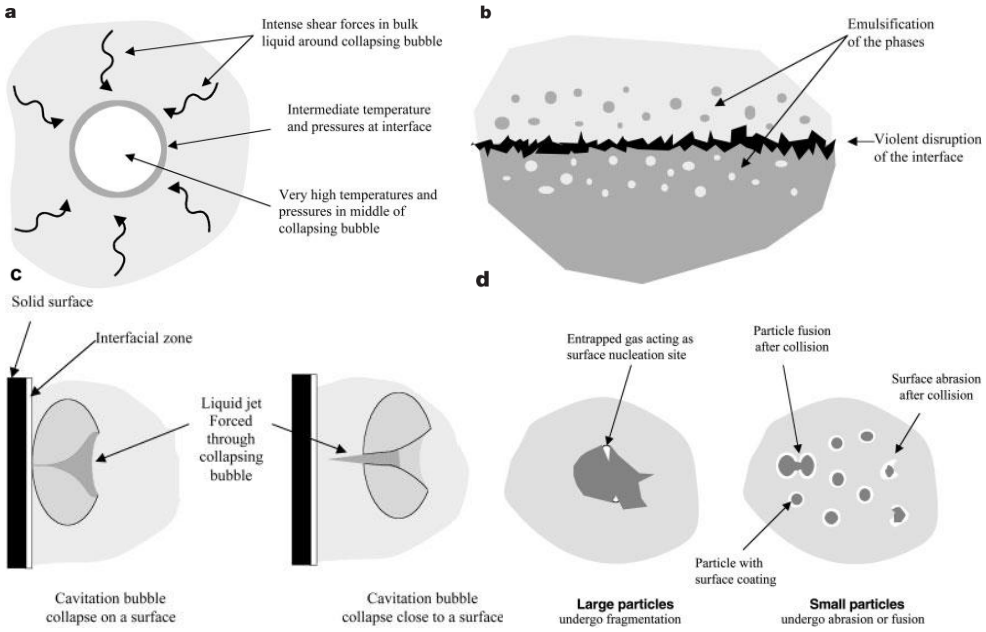

Figure 2.14 Effects of sonication in a **(a)** homogeneous liquid phase **(b)** biphasic liquid system **(c)** liquid near to a solid surface **(d)** liquid containing suspended particles. (Reproduced from (*59*), Copyright 2002, Wiley-VCH)

2.2.2 Sono-synthesis of Polymers and Hydrogels

Based on the fundamental understanding of sonochemistry, ultrasound has been involved in chemical synthesis as an alternative energy source.(*60, 61*) It's considered an accessible, clean, and sustainable energy, supporting multimode adjustments. In comparison to small-molecule reactions, the distinctive mechanochemical effects induced by acoustic cavitation seem to enable coupling with polymer strands to a larger extent. For one thing, free-radical polymerization is a widely applied technique in polymer synthesis, while homogenous sonochemistry can initiate the production of free radicals in regular ambient conditions. For another, the shearing-triggered mechanoradicals are promising new growing points to construct new polymer chains or networks. (*52, 62*) By incorporating specific mechanophores, site-specific scissions could be realized, offering attractive functionality and applicability. For instance, Torkelson et.al. investigated the application of high-intensity ultrasound in block

copolymer synthesis. (*63*) Fluorophore-labelled gel permeation chromatography (GPC) proved the formation of block copolymers from two different mechanoradicals in a mixed polymer solution, which only took several minutes. The high energy release rate of ultrasound makes it outstanding in industrial production.

Previous studies validated the universality of sono-synthesis in diverse polymerization settings, including both free-radical and controlled polymerization. For free-radical polymerization, small molecules like solvent molecules, either aqueous or organic solvent, can serve as the spontaneous supply source of free radicals. Kinetic studies by Price et.al. (*64, 65*) and Kruus et.al. (*66*) revealed the effect of ultrasound parameters as well as solution composition on the rate of radical formation and initiation. According to their proposed mechanisms, the sonochemical radical polymerization contains the following series of reactions (as shown in Figure 2),

$$\mathrm{M} + \mathrm{C} \xrightarrow{k_1} \mathrm{R}^{\bullet} \tag{2}$$

$$\mathrm{R}^{\bullet} + \mathrm{M} \xrightarrow{k_2} \mathrm{R}_1^{\bullet} \tag{3}$$

$$\mathrm{R}_1^{\bullet} + \mathrm{nM} \xrightarrow{k_\mathrm{P}} \mathrm{R}_\mathrm{n}^{\bullet} \tag{4}$$

$$\mathrm{R}_\mathrm{m}^{\bullet} + \mathrm{R}_\mathrm{n}^{\bullet} \xrightarrow{k_\mathrm{t}} \mathrm{P} \tag{5}$$

$$\mathrm{P} + \mathrm{C} \xrightarrow{k_3} 2\mathrm{R}_\mathrm{n}^{\bullet} \tag{6}$$

generation of small-molecule radicals, initiation, propagation, termination, and chain scission (or production of mechanoradicals). (*59*) By applying the classic steady-state analysis, the dependence of propagation rate turns out to be the square root of the acoustic intensity. In addition, acoustic initiation shows obvious independence of temperature, which is essentially different from thermal polymerization. As explained before, acoustic cavitation favors the formation of emulsion. The synthesis of several industrial polymers has been involved in

ultrasound-induced emulsion polymerization, such as polystyrene, poly(methyl methacrylate) (*67*), poly(acrylonitrile) (*68*), etc. On the other hand, ultrasound could also synergize controlled radical polymerization. Qiao et.al. developed a sonochemically induced reversible addition-fragmentation chain-transfer (RAFT) polymerization of methyl acrylates and acrylamide. (*69*) The instant control toward ultrasound can act as a switch to determine the generation of hydroxyl radicals that initiate the reaction. Another study reported by Matyjaszewski et.al. utilized the same hydroxyl radical but in the sono-atom transfer radical polymerization (ATRP). (*70*) These sonochemically formed radicals fulfill the role of reducing agents to convert the inert oxidized copper (II) catalyst to activated copper (I) species. The strategy was successfully applied to 2-hydroxyethyl acrylate, poly(ethylene glycol) methyl ether methacrylate (*71*), etc. even with a high molecular weight of over 100 kDa.

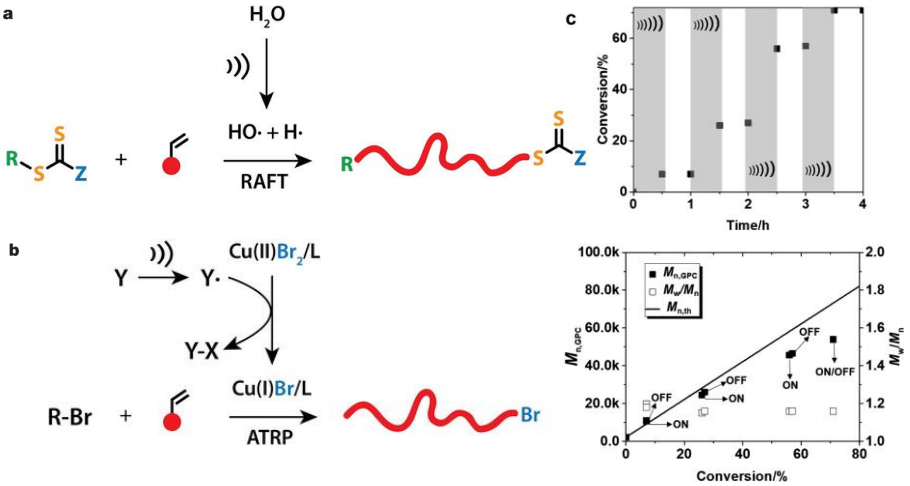

Figure 2.15 Scheme for sonochemically induced **(a)** RAFT polymerization **(b)** ATRP reaction by radical reduction of $Cu^{II}Br2$ (deactivator) complex to $Cu^{I}Br$ (activator) by sonochemically derived radicals. (Reproduced from (*52*), Copyright 2019, Wiley-VCH) **(c)** Temporal control in aqueous sono-ATRP of oligo(ethylene oxide) methyl ether methacrylate under ultrasound agitation through intermittent switching on/off the ultrasound bath. (Reproduced from (*70*), Copyright 2018, ACS)

Unlike straight synthesis of polymers, the construction of swollen polymer networks or hydrogels has been rarely reported by ultrasound. Representative examples include the study of Ulanski et.al. on PEGDA family hydrogels and Cass et.al. on HEMA hydrogels. In 2009, Ulanski and colleagues investigated the macroscopic gelation kinetics of covalently crosslinked PEGDA hydrogels, in particular the effects of acoustic frequency, substrate concentration, and sonication time on gel fraction. (*72*) They attributed the formation of sonogels to water-cleaved hydroxyl radicals, which are most effectively generated at a middle frequency (600 kHz). Research from the Cass group also focused on the conversion rate of sonogel synthesis. (*73*) They took quantitative infrared spectra and swelling tests and studied the effect of glycerol and sonication time. Besides, Yang et.al. reported hydrogel formation by ultrasound-triggered thiol-norbornene crosslink. They built basic relationships between sonication conditions and the microstructure of the resulting hydrogels. (*74*) However, given the substantial difference between ultrasound and other preparation methodologies, there still exists a significant knowledge vacancy in the synthesis-property relationship of sonogels. Moreover, no direct clear evidence was explored to corroborate mechanisms of sonochemical gelation, which are essential to accommodate their further use in advanced fabrication or biomaterials engineering as introduced below.

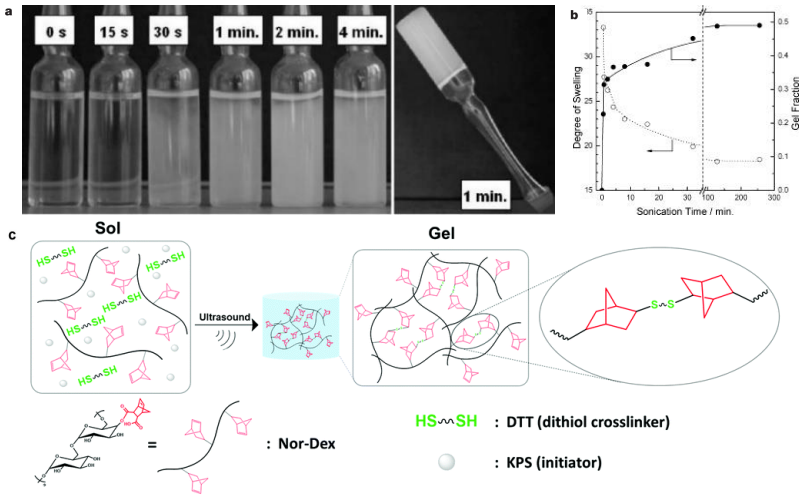

Figure 2.16 (a-b) Sonication (622 kHz, 75 W kg−1) of Ar-saturated aqueous solutions of PEGDA (10% w/v). **(a)** Formation of macroscopic, covalent gel as a function of sonication

time. **(b)** Gel fraction and equilibrium degree of swelling of the gel as a function of sonication time. (Reproduced from (*72*), Copyright 2009, ACS) **(c)** Norbornene-dextran hydrogel formation through the ultrasound-initiated thiol–norbornene reaction between it and dithiothreitol. (Reproduced from (*74*), Copyright 2022, RSC)

2.2.3 Advanced Applications of Ultrasound in Soft Materials

Given the potential diversity, creativity, and reactivity of ultrasound, there are some advanced applications of sono technologies emerging in hydrogel fabrication or soft matter engineering. Ma et.al. reported the straightforward function of ultrasound in enhancing tough bioadhesion with hydrogels. (*75*) The strong cavitation effect and microstreaming propel and immobilize the anchoring agents (or bridging polymers) deep into tissues. The dynamic topological adhesion avoids surface modification and potential toxicity induced by chemical agents. Unlike the negatively controlled group, ultrasound-mediated bioadhesion improved by over 15 times and obtained adhesion energy of around 1750 J m^{-2} on porcine skins. Cyclic tensile tests showed a high fatigue threshold of ultrasound-treated groups, which was attributed to the existence of strong interfacial interactions between anchoring polymers and tissues. Moreover, this bioadhesion is spatially and temporally controlled, and its profile is profoundly determined by the distance between the transducer and the tissue or the nature of the hydrogel patch.

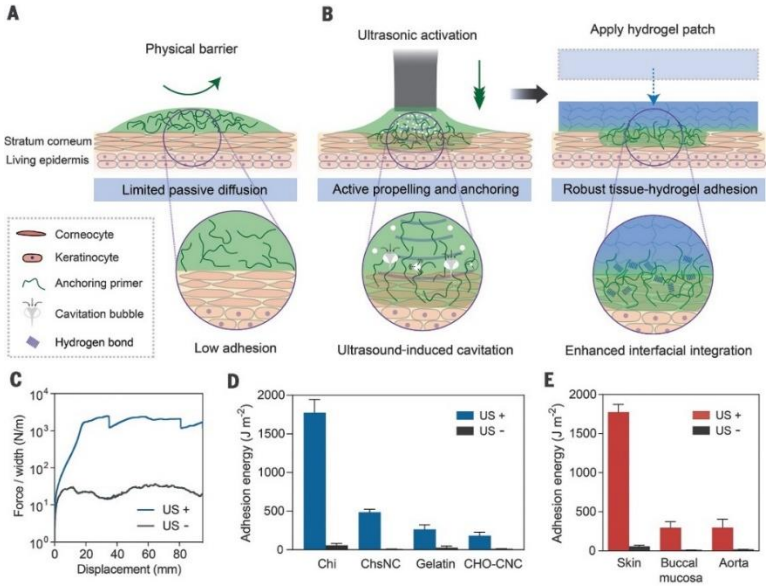

Figure 2.17 Robust and versatile ultrasound-mediated tough bioadhesion. **(A)** Schematic of

skin with barrier effects limiting passive diffusion and impairing bioadhesion. **(B)** US actively propels and anchors primer agents into a tissue substrate, causing spatially confined tough bioadhesion. **(C)** Representative force-displacement curves of hydrogel-tissue (porcine skin) hybrids with or without US treatment in peeling tests. Wide applicability of the method with **(D)** diverse anchoring agents and **(E)** diverse biological tissues.(*75*) (Copyright 2022, AAAS)

Apart from coupling with bioadhesion, ultrasound also has been proved potential in 3D printing-represented advanced manufacturing of soft materials. In 2022, Habibi et.al. prototyped the first sono-printing systems for elastomers by utilizing cavitation-driven sonochemical reactions. (*76*) They used high-intensity focused ultrasound (HIFU) to build an ultra-active microreactor, where the deposited liquid resin got solidified rapidly under the short-lived thermal energy. By adjusting the transducer driving pulse, building materials, and transducer motion, different microstructures and resolutions of elastomer patterns could be printed. High-speed imaging revealed the dynamic physical transformation from liquid resin to cured elastomers, particularly the variation of acoustic pressure and resin density. The deep penetration of acoustic energy makes it possible for remote distance printing, offering an alternative option for non-invasive bioprinting of tissues or organs (such as ear and nose) in the medical field.

Following this study, Kuang et.al. reported acoustic volumetric printing of hydrogels recently and further pushed this technology into practical biomedical applications. (*77*) They innovated self-enhancing sono-inks, which prevented acoustic streaming-induced low resolution and geometric fidelity while supporting rapid sonothermal polymerization and a deep printing depth simultaneously. The sonoink consists of acrylate oligomer (PEGDA), acoustic absorber (agar microparticles), rheology modifier (PNIPAM), as well as thermal initiators (APS). From rheological curves, the sono-ink shows characteristic shear-thinning behavior, favoring deep acoustic penetration under high-frequency acoustic waves. On the other hand, the phase transition of PNIPAM with a rising temperature leads to significant increasing of ink viscosity,

which cushions intense streaming effectively and guarantees a good resolution. At optimal ultrasound frequency and scanning speed, the in-plane curing size could decrease to 1.6 mm.

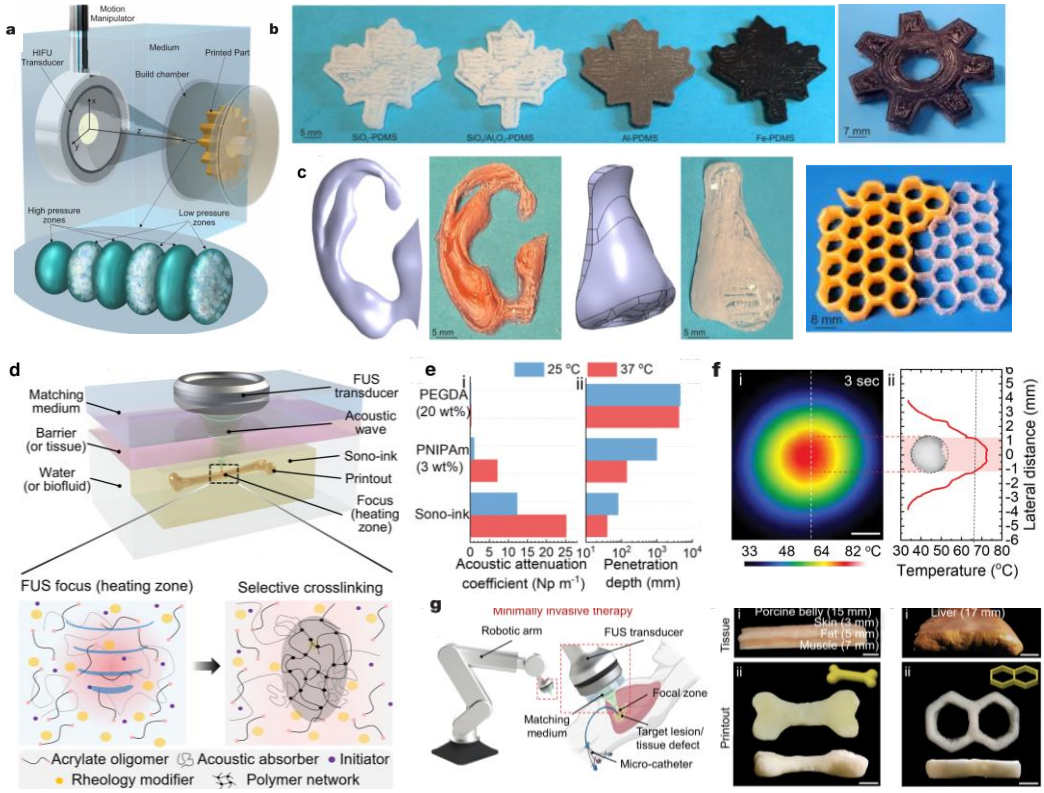

Figure 2.18 (a) Schematic of the direct sound printing (DSP) system. **(b)** Printing opaque micro/nano composites by DSP. **(c)** printed ear and nose using the tissue phantom. **(d)** Scheme showing acoustic printing of constructs by selective curing of sono-ink using deep-penetration FUS. (Reproduced from (*76*), Copyright 2022, Spring Nature) **(e)** Acoustic properties of the PEGDA/agar/PNIPAm sono-ink and its acoustic attenuation coefficient and penetration depth under 3.41-MHz FUS at 25° and 37°C. **(f)** Typical surface temperature profile near the FUS focal region. **(g)** Scheme of minimally invasive therapy by through-tissue manufacturing of scaffolds on target lesions and tissues, including bones and liver. (Reproduced from (*77*), Copyright 2023, AAAS)

Chapter 3. Methodology

3.1. Materials

Acrylamide (AAm, A8887), glycerol (G9012), Poly(ethylene glycol diacrylate) (PEGDA, Mn = 700 g mol^{-1}), Poly(vinyl alcohol) (PVA, Mw 31000-50000 g mol^{-1}), acrylic acid (AAc, 8.00181), low-molecular-weight chitosan, calcium chloride dihydrate ($CaCl_2 \cdot 2H_2O$), ammonium persulfate (APS), and α-ketoglutaric acid were purchased from Sigma-Aldrich. Sodium alginate (I1G) was purchased from Kimica Inc. 5,5-Dimethyl-1-pyrroline N-oxide (DMPO) was purchased from TCI Chemicals Inc. All chemicals were used without further purification.

3.2. Experimental Section

Preparation of PAAm-alginate tough sonogels

For sonogels of the standard group, alginate is dissolved in deionized (DI) water at 2.256% (w/v) first. Add the same mass of glycerol as water to get the mixed solvent. Dissolve 19.33% (w/w) of acrylamide monomers and 0.67% (w/w) of PEGDA crosslinkers (φ_m = 29) and stir overnight to obtain a clear solution. The precursor is fully degassed in the vacuum chamber before sonication. Cut the tip of a 30ml syringe to make it an open container and load 3 grams of precursor solution in it every time to keep batch-to-batch consistency. Fill a large beaker with enough ice water and make sure the precursors are completely submerged in the bath. Immerse the sonication probe (VWR International LLC.) into the precursors and fix its location when the probe tip (0.94mm diameter) is approximately 1mm under the liquid level. Set the US intensity as 56 W cm^{-2} (30% power) and sonication time as 2min, 3min, 4min, 6min, or 8min (in the measurement of gelation profiles), respectively. The temperature profiles of the sonication system were measured with an infrared thermal camera. The completion of sonogel

formation is usually accompanied by noise diminishing, which could serve as an intuitive mark to judge the reaction progress. After the sonication is finished, use Kimwipe (Kimtech Science TM.) to swipe the remaining solution on the gel surface, and record its net weight. Place the gel in the 0.05M $CaCl_2$ solution and post-crosslink for 2 hours to get the DN sonogel. Fourier transform infrared (FTIR) analysis was conducted by Spectrum II (Perkin Elmer) to confirm the polymerization of vinyl monomers during sonication.

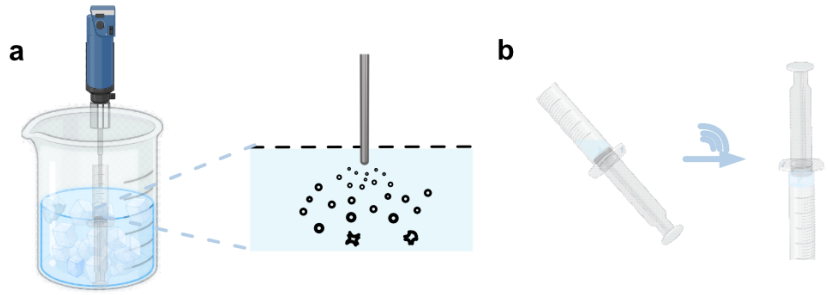

Figure 3.1 (a) Schematic of the experimental setup for sonogel synthesis. Cavitation bubbles are generated and diffused in the liquid media. **(b)** The formation of bulk gels inside the syringe after sonication.

Preparation of other DN sonogels

For PAAc-alginate DN sonogels, prepare the same alginate solution with the mixed solvent. Add 29% (w/w) of AAc monomers and 1% (w/w) of PEGDA crosslinkers (φ_m = 29) and mix well to get the precursor solution. Repeat the same sonication (with 5 minutes of sonication) and post-crosslinking steps.

For PAAm-PVA DN sonogels, weigh 10% (w/v) PVA into DI water and put it in the 90°C oven for 1 hour to dissolve. Follow the above steps until the gelation transformation finishes (with 8 minutes of sonication). Freeze and thaw sonogels three times to facilitate the formation of crystalline regions between PVA chains to post-crosslink that network.

For PAAm-chitosan DN sonogels, dissolved low-molecular-weight chitosan (2% w/v) in DI

water with 200 μL CH_3COOH. Follow the above steps until the gelation transformation finishes (with 4 minutes of sonication). Place the as-prepared sonogel in 1M Na_2SO_4 solution and post-crosslink for 12 hours.

Effects of precursor composition

To study the effect of glycerol ratios, prepare mixed solvents with the mass ratio of glycerol (φ_g) as 25%, 40%, 50%, and 60% respectively, and then dissolve alginate at the concentration of 1.128% (w/w). Add 19.33% (w/w) of acrylamide monomers and 0.67% (w/w) of PEGDA crosslinkers (φ_m = 29) and stir overnight to obtain a clear solution. For the gelation profiles at varying solvent composition, sonicate 3g of precursor solution for 2 min, 3 min, 4 min, 6 min, and 8 min respectively, and measure the compression modulus of the as-prepared sonogels. For the fracture energy, all the precursors were sonicated for 4 minutes to ensure the completion of macroscopic gelation transformation. The sonogels were post-crosslinked in 0.05 M $CaCl_2$ solution for 2 hours and then measured by 180-degree peeling tests.

To study the effect of monomer-to-crosslinker ratios, dissolve alginate (1.128% w/w) into the mixed solvent (where the mass ratio of water/glycerol is 3/2). Add acrylamide monomers and PEGDA crosslinkers as 19.67%/0.33% (w/w, φ_m =59), 19.33%/0.67% (w/w, φ_m =29), 19%/1% (w/w, φ_m =19), and 18.67%/1.33% (w/w, φ_m =14) respectively. All the precursors were sonicated for 4 minutes to ensure the completion of macroscopic gelation transformation. The sonogels were post-crosslinked in 0.05 M $CaCl_2$ solution for 2 hours and then measured by 180-degree peeling tests.

High-speed and polarized imaging for direct visualization.

The high-speed imaging platform is shown in the schematic in **Figure 3.2**. The high-speed camera comes from Nikon AF-S Nikkor 60mm f/2.8G ED, fixed on a motion controller to be

moved laterally to achieve focus. The chamber to contain precursors has a symmetric sandwich structure, including acrylic sheets, rubber gaskets, and a 3D-printed mold from outside to inside sequentially, where rubber gaskets ensure no leakage of solution during sonication and layers are fixed together with screws. The internal size of the chamber is 4×1×6 mm^3 and there is a hole of 0.94cm diameter (3/8 inch) on the lid allowing the sonicator probe to immerse into the solution. A working LED light bulb (5500 Lumen) is placed behind the chamber to eliminate light noise from the background. The camera footage, precursor solution, and light bulb are aligned horizontally before measurement. Imaging tests went on the Photron FASTCAM View 4 (PFV4). After building connections between the camera and the software, set the frame rate as 2000 fps, shutter speed as 1/80000 second, and resolution as 512 × 512 pixels.

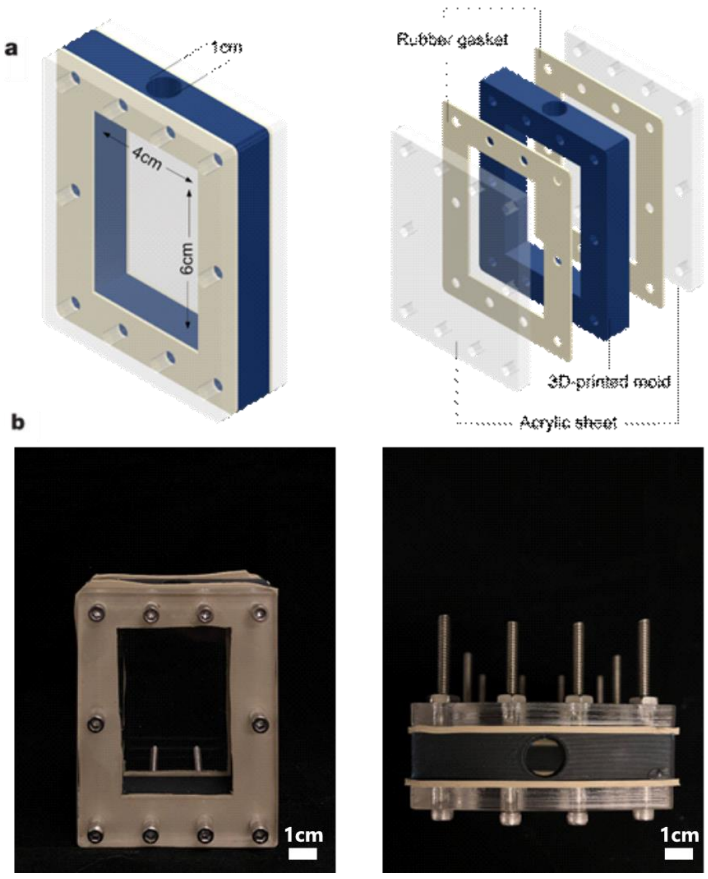

Figure 3.2 (a) Schematic and **(b)** Physical side views of the designed chamber for high-speed imaging

Fill the chamber with fully degassed precursor solution and immerse the probe tip into it at a 2mm depth. After starting sonication, screenshots and videos are taken every 2 minutes to

record the dynamic changes during reaction progress. Original images were processed by ImageJ to get the binary images of cavitation clouds for quantitative analysis.

In polarized imaging, we replaced acrylic with a glass container of the same size. The glass sheets were directly adhered to the 3D printed mold using silicone glue. Unlike acrylic that may exhibit birefringence and introduce artifacts and distortions to interfere polarized imaging, glass behaves more stable and consistent optically. To attain high-quality polarized images, bipolarized filters were applied in the system (**Figure 3.3**), including a linear polarized filter placed between the light source and the glass container as well as a circular polarized filter embedded on the camera footage.

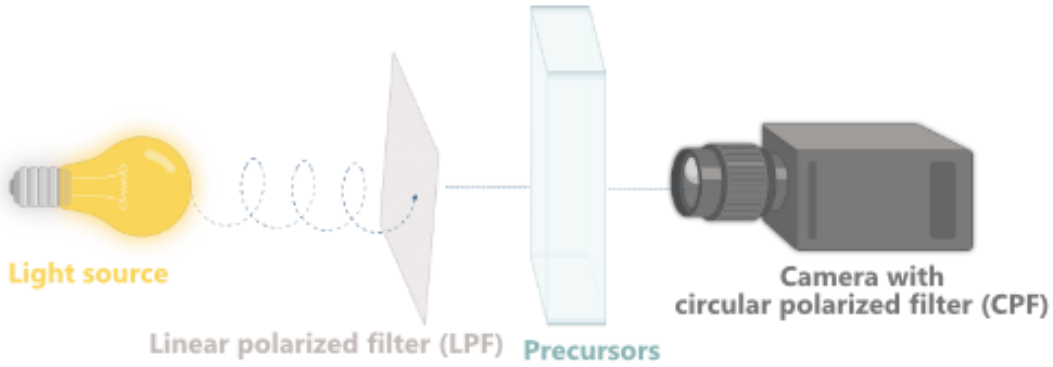

Figure 3.3 Schematic of the experimental setting for polarized imaging.

Rheology measurements of sonogels

The plateau shear modulus and frequency sweep of PAAm-alginate sonogels prepared under various ultrasound intensities were measured using a rheometer (DHR-3, TA Instruments). The as-prepared sonogels were cut into dish-like samples with a diameter of 20 mm and directly sent to rheology tests without post-crosslinking. A flat steel plate of the same diameter was adopted, and silicone oil was applied at the edge of the sample to prevent evaporation. The measurement included two consecutive programs, an initial time sweep to characterize the plateau shear modulus followed by a frequency sweep to check the viscoelasticity of sonogels. The time sweep lasted for 10 minutes with an oscillation strain rate of 0.1% and frequency of 1Hz, while in the frequency sweep, the range of oscillation frequency was set between 10^{-3} ~

10^2 Hz with 20 points recorded at each interval. Both programs were carried out under room temperature (23°C). Storage modulus (G′), loss modulus (G″), and other relevant parameters were recorded.

Measurement of mechanical properties

All mechanical tests were conducted with an Instron machine while recording the primitive force and displacement. Compression tests were performed to characterize the elastic modulus (*E*) of sonogels. To describe the gelation profiles under various ultrasound intensities or with different glycerol amounts, sonogels were measured without post-crosslinking. The dimensions of each sample were ≈ 20 mm in diameter by ≈ 6 mm in thickness. For the kinetics of the post-crosslink process, sonogels were measured at 10min, 20min, 30min, 60min, and 120min respectively after being immersed in $CaCl_2$ solution of corresponding concentrations. In each case, the unidirectional loading rate was kept constant at 0.01 mm/s and the maximum displacement was 1 mm. The elastic modulus was calculated from an initial slope of a stress-strain curve ($\lambda < 0.05$).

To measure the toughness, 180-degree peeling tests were performed. Post-crosslinked sonogels were cut into rectangular samples of ≈ 20 mm (length) × 8 mm (width) × 3 mm (thickness) and then attached to rigid polyethylene terephthalate (PET) films using Krazy glues to prevent axial deformation during testing. A 3mm precrack was given by sharp razors to create a notched sample, and the free end of the sonogel was then fixed with mechanical grips. The Instron applied unidirectional tension at a constant loading rate of 0.5 mm/s. The fracture energy was

calculated as two times of the plateau value of the ratio of the force and width.

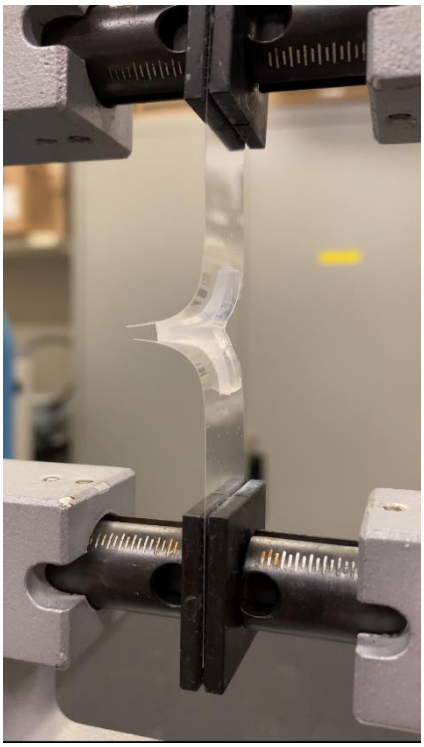

Figure 3.4 180-degree peeling tests to measure the fracture energy of post-crosslinked sonogels.

EPR study for radical measurement

To reveal the nature and origin of initiator species during sonogel synthesis, qualitative EPR measurements were performed with a Bruker Elexsys E580 X-band EPR Spectrometer. The spin trap (DMPO) concentration in the precursor solution was 10 mg/ml. (*78, 79*) Provided that the highly viscous precursor was hard to fast transfer into the 3mm long quartz EPR tubes possibly leading to the decomposition of spin adducts, all samples were loaded into a short glass capillary of 1mm diameter right after 1min sonication, and then sent to a 3mm quartz tube for EPR measurement. The microwave and modulation frequencies were 9.86 GHz and 100 kHz respectively, while the microwave power level was set at 16.50 mW with an attenuation of 11 dB. Future parameters are given below in **Table 3.1**. All spectra were recorded at room temperature and each group was repeated three times for consistency. The experimental spectra were simulated using the SpinFit module in the Bruker Xepr software to offer information about the g factor as well as hyperfine coupling constants to nitrogen (α_N) and

hydrogen (α_H) for identifying the trapped radicals.

Table 3. 1 Electron paramagnetic resonance experimental parameters

Parameter	Unit	Value
Microwave frequency	GHz	9.8
Modulation frequency	kHz	100
Attenuation	dB	11
Microwave power	mW	16
Modulation amplitude	G	1
Time constant	s	327.68
Conversion time	s	655.36
Sweep time	s	671.08
Number of scans	—	1
Center field	G	3510
Sweep width	G	100

SEM images

Scanning electron microscopy (SEM) was performed on hydrogels prepared from various initiation methods. The composition of all gels was the same as introduced above in the preparation of sonogels. For the room temperature group, the precursor solution was injected into a closed glass mold and cured for a week. For the room temperature group, the precursor solution was straight injected into a closed glass mold of 46×20×3 mm^3 and cured for a week. For thermal-initiated hydrogels, 0.5% (w/w) APS was mixed into the precursor before being clamped in the mold, and then cured in the 40°C oven for 8 hrs. As to photo-initiated hydrogels, 0.5% (w/w) α-ketoglutaric acid was added into the solution while the mixture was subsequently subject to UV irradiation (OAI Instruments, 33 mW cm^{-2}, 365nm) in an ice bath for 1 hr.

The microstructure of hydrogels was imaged using a focused ion beam-extreme high-resolution SEM (FEI Helios Nanolab 660). All the samples were solvent exchanged through gradient concentrations of anhydrous ethanol (30%, 50%, 70%, 80%, 90%, and 100% v/v) and then

dehydrated using a CO_2 supercritical point dryer (CPD030, Leica) to preserve the original pore size. The dehydrated samples were coated 5 nm Platinum using a high-resolution sputter coater (ACE600, Leica) to increase surface conductivity. The porosity of samples was analysed by ImageJ.

Chapter 4. Results and Discussion

4.1. Preparation of Tough Sonogels

The toughening strategies for hydrogels usually include the construction of double networks, incorporation of fibers or functional , as well as introduction of monodispersed long polymer chains. Considering the polymerization process involved in sono-synthesis, we employed the classic double-network hydrogel here of (poly)acrylamide (PAAm) and alginate (Alg). PEGDA (Mw=700 g/mol) and glycerol were added into precursors as crosslinkers (φ_m = 29) and co-solvent additives (φ_g = 50%) respectively. The default US frequency and intensity were 20kHz and 56 W cm^{-2} respectively. As the schematic (**Figure 4.1**) illustrates, the probe sonicator remains immersed in the solution and the reaction goes without a strict oxygen-free environment. To circumvent thermal effects and keep the bulk temperature constant, the whole experiment was conducted in the ice-water bath. A thermal infrared thermometer was

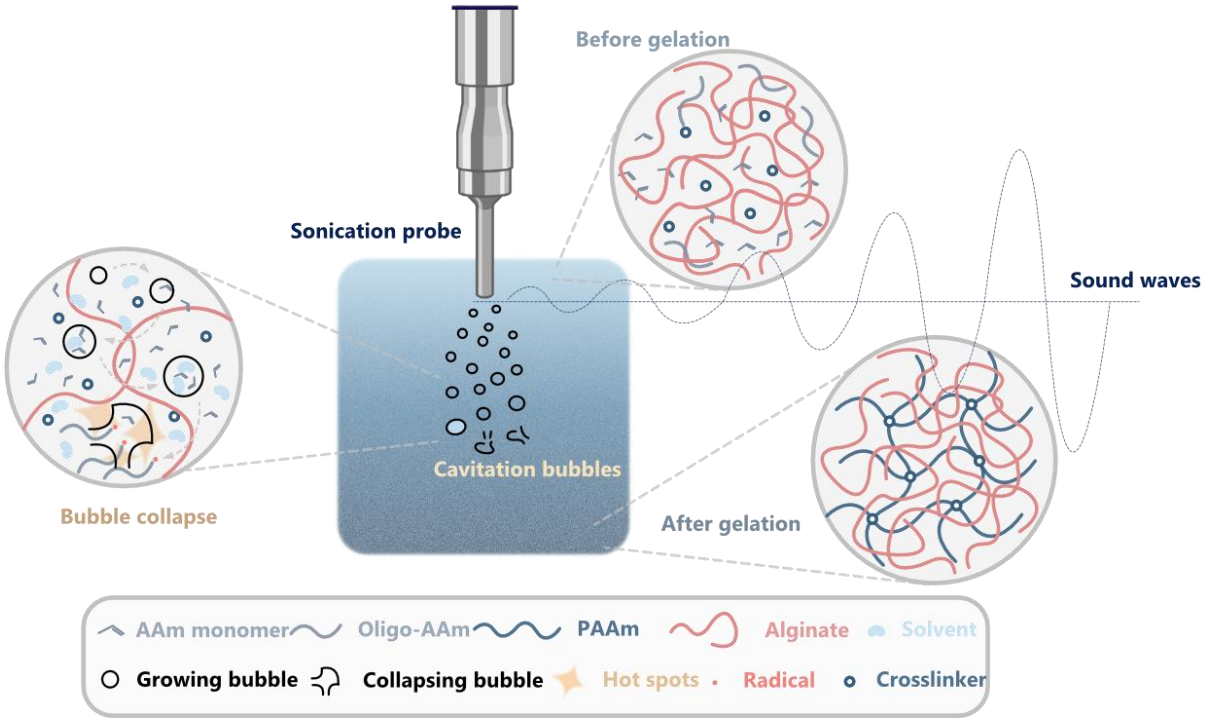

Figure 4.1 Schematic of the sonochemical polymerization and gelation process. Imploded cavitation bubbles (hot spots) initiate the homolytic cleavage of small molecules and the resulting free radicals further induce the propagation of monomers followed by crosslinking

into a network.

employed to monitor the real-time temperature, which stayed around 0°C in the peripheral and rose to 35-40°C in the center after a 4-minute application of 56 W cm^{-2} US (**Supplementary Figure 4.9**). The as-prepared sonogel shows excellent optical transparency (**Figure 4.2a**), and FTIR spectra endorsed successful polymerization of acrylamide monomers. We did rheology tests to evaluate its viscoelasticity characteristics. As expected, within the scanned frequency range, the storage modulus (G′) remained consistently greater than the loss modulus (G″). (**Figure 4.2b**) Below 10^{-2}-10^{-1} Hz, G′showed significant frequency independence, when merely load-bearing strands contributed to the modulus while the viscoelasticity induced by dangling chains or other defect units was released.

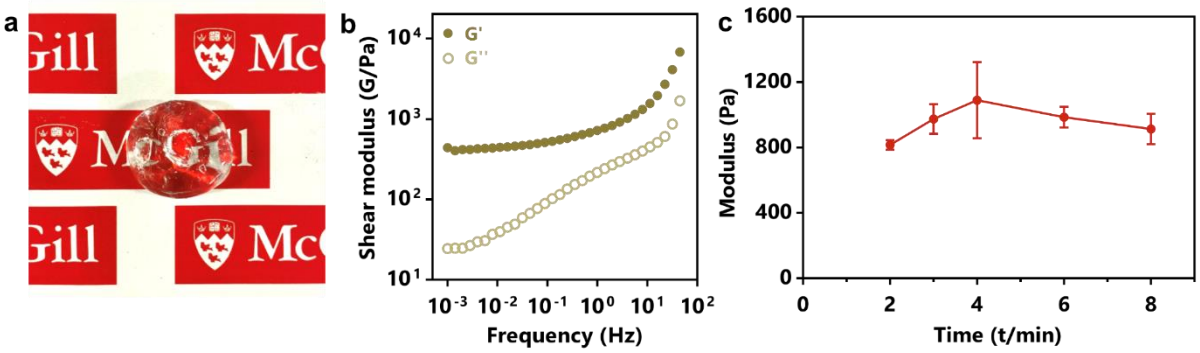

Figure 4.2 (a) The digital image of PAAm-alginate double network sonogel. **(b)** The storage and loss moduli as functions of frequency for as-prepared sonogels. **(c)** The compression-modulus relationship (gelation profile) of sonogels prepared under 20kHz, 56 W cm^{-2} US for different time periods.

We further measured its compression modulus at various sonication time intervals to characterize the reaction progress and gelation efficiency. (**Figure 4.2c**) The average sample thickness was 6mm and the loading rate was 0.01mm s-1, ensuring all contributions to the modulus originate from elastic networks formed from sonication. It turned out that 3g of precursor solution could transform into a gel within merely 2 minutes, performing an entirely distinct kinetic behavior compared with conventional hydrogel preparation processes. The

sonogel kept strengthening under continuous sonication and reached its peak modulus at around 4 minutes. Further irradiation led to a decline of modulus, which could be attributed to the internal damping of hydrogel networks that some long end-crosslinked polymer chains got scissioned by cavitation-induced shear forces.

The sonication process concurrently involves diffusion of cavitation bubbles, intense liquid streaming, and transition from homogeneous to heterogeneous systems. To build a more intuitive understanding of the mechanochemical impact of cavitation in the course of gelation, we conducted a series of real-time imaging tests, including high-speed imaging and polarized imaging. For high-speed imaging, we designed an acrylic-made, sandwich-structured chamber for containing precursors. The chamber had an inner size of $4\times1\times6$ mm^3, with transparent front and back sides for observation. Videos and images were recorded every 2 minutes to record the continuous dynamic changes occurring inside. As shown in **Figure 4.3a**, only cavitation clouds with a diameter of approximately 2cm were observed initially. With the reaction going on, more visible dark spots appeared increasingly and started gathering near the probe tip, reflected as an increasing cloud density in the binary images (**Figure 4.3b**). At 6 minutes, more dark spots began to show up and moved around with the streaming counterclockwise. When further tracking those spots, we found some split into smaller ones and stayed at fixed locations to form a boundary. The acute noise of low-frequency US also diminished and eventually disappeared, indicating the completion of gel transformation. To figure out the essence and origin of dark spots, polarized filters were applied to enhance visual contrasts. After emission from the source, light first passes a linear polarized filter (LPF). The polarized light would get refracted or scattered when going through the forming polymer network. When it reaches the circular polarized filter (CPF) over the footage, an apparent color difference would be observed on the display to indicate the region where the gelation transformation has been occurring. It turned out that the visible dark spots were the growing and diffusing bubbles. With the

formation of bulk gels, some bubbles got trapped near the sol-gel boundary and appeared dark due to the scattering of light. In combination with the high-speed and polarized imaging, we could monitor the gelation transformation in a real-time manner.

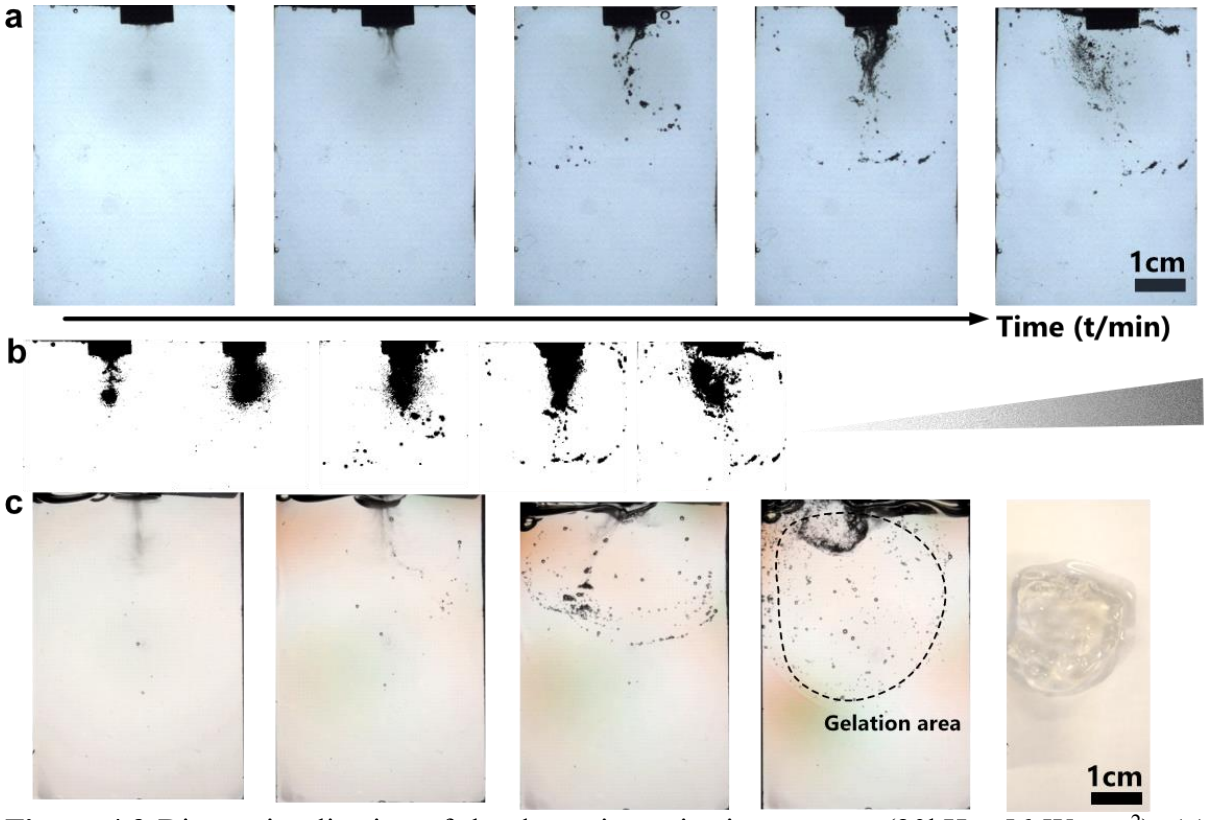

Figure 4.3 Direct visualization of the dynamic sonication process (20kHz, 56 W cm^{-2}). **(a)** High-speed imaging of the precursor solution at 2 min, 4 min, 6 min, 8 min, and 10 min respectively. **(b)** Processed binary images indicating the increasing density of bubble clouds. **(c)** Polarized imaging of the precursor solution at 2 min, 4 min, 6 min, 8 min and the resulting piece of sonogel, whose shape exactly matched the gelation area surrounded by dark spots. (scale bar: 1cm)

The as-prepared sonogel has only one covalently crosslinked network. To make inter-penetrated DN gels, we post-crosslink alginate in a calcium chloride ($CaCl_2$) solution. We first studied post-crosslinking kinetics to confirm the optimal calcium concentration and post-crosslinking time by measuring the bulk modulus. All gels were cut into the same geometry in advance, whose volume was negligible in comparison to the solution, so as changes of Ca^{2+} concentration. Results showed that in solutions with a higher Ca^{2+} concentration (0.5M), the hydrogel stiffness would get a more rapid increase in the beginning and reach a plateau earlier,

while the equilibrium modulus is lower than those immersed in 0.1M and 0.05M solution. As migration of Ca^{2+} simply relies on free diffusion, the gel surface is always more likely to get post-crosslinked earlier than the inner bulk, and therefore a higher initial concentration tends to constrain inward migration of ions after the surface gets post-crosslinked. In contrast, Ca^{2+} enters into hydrogels in a more even and slower manner in the 0.05M group, and the resulting samples performed a more uniform structure and property. We did 180° peeling tests to measure the fracture energy of hydrogels after 2 hours of post-crosslinking, and the results illuminated that samples from the lowest Ca^{2+} concentration group did have the largest fracture energy of around 300 J m^{-2} on average.

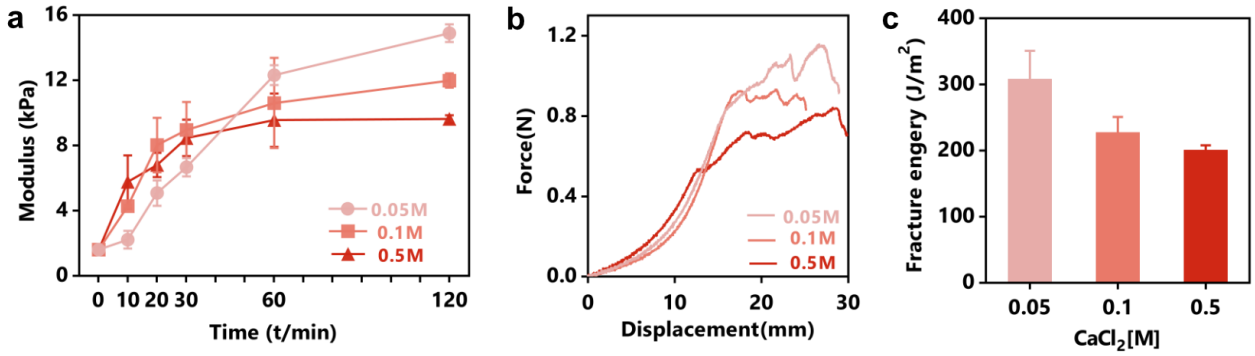

Figure 4.4 Post-crosslinking of PAAm-alginate DN sonogels. **(a)** The post-crosslinking kinetics of sonogels in varying concentrations of $CaCl_2$ solution. (circle 0.05 M, square 0.1 M, triangle 0.5 M) **(b)** Force-displacement curves of the post-crosslinked sonogels at 180-degree peeling tests. (sample width 8 mm) **(c)** Fracture energy of post-crosslinked sonogels. (light red 0.05 M, red 0.1 M, dark red 0.5 M)

4.2. Mechanism Study by EPR Spectra and Reaction Progress

Although several examples of sonogels have been reported before, we still know little about the underlying gelation mechanism. According to classic sonochemistry theory, imploded cavities (or hot spots) generated from acoustic cavitation are direct sources to induce cascade sonochemical reactions, including homolytic cleavage of small molecules, and diffusion and reaction of the resulting free radicals. As a direct measurement technique for free radicals, EPR

spectroscopy offers high sensitivity, specificity, fast time resolution, and compatibility with broad test conditions. Here, we did ex-situ EPR with DMPO as a spin trap reagent. We first tested the standard sample before and after sonication as illustrated in **Figure 4.5a**. A triplet signal with a hyperfine constant of α_N = 15.7G was observed in the unsonicated sample, which belonged to the decomposition products of DMPO itself. After 1 minute of ultrasound irradiation, two groups of symmetric peaks appeared, including DMPO•-OH and DMPO•-R. The DMPO•-OH spin adducts showed a symbolic four-line peak with an intensity ratio of 1:2:2:1, while DMPO•-R consisted of six-line peaks of similar intensities. Due to a smaller hyperfine coupling to nitrogen (I = 1, α_N = 15.3G) than to hydrogen (I = ½, α_H^β = 22.7G), R was supposed to be a relatively stable carbon radical with one β-H. (*79, 80*) Measurement results of radical stability also supported this assumption, where the sample after 90 minutes of sonication only showed a decreased level of DMPO•-R while DMPO•-OH decayed completely. In addition, the signal intensity of the sonicated sample was far higher than the control group, which confirmed the effect of cavitation in accelerating the production of initiator species. Spin adducts of other reactive oxygen species (ROS) didn't get captured obviously, which could be attributed to their intrinsic instability. (*81-83*) In principle, nearly all species could diffuse into the growing cavitation bubble and cleave into reactive radicals during homogeneous sonochemistry as they were all small molecules. To further identify the chemical essence of R species and figure out which radical plays a substantial role in facilitating gelation, we compared the spectra of different samples. (**Figure 4.5b-d**) Only noise were detected before sonication in all three groups. For water alone, hydroxyl radicals were captured evidently after sonication, indicating the primary source of DMPO•-OH in the precursor solution. After mixing with glycerol, the same spectrum pattern to the standard sample occurred, and we inferred the R species was practically the hydroxyalkyl radicals ($^\bullet CH_2OH$, $^\bullet CH(OH)CH_2OH$, or $^\bullet CH_2CH(OH)CH_2OH$) from glycerol. As the intensity of DMPO•-OH signal declined so

remarkably as to lower than that of DMPO•-R compared with the former group, we assumed these hydroxyalkyl radicals were generated from cascade reactions between hydroxyl radicals and glycerol molecules. Likewise, the spectrum showed familiar changes with the standard group during the post-sonication decay. When acrylamide and alginate were dissolved in pure water, two groups of similar signals also illustrated but notably, the DMPO•-R was much less intense than DMPO•-OH. The fitting spectrum informed a pair of deviated hyperfine coupling constants, α_N 15.5G and α_H^β = 22.8G respectively, referring to alkyl radicals from acrylamide monomers. The slight difference makes it challenging to distinguish separate contributions of DMPO•-R from either acrylamide-induced alkyl radicals or glycerol-supplied hydroxyalkyl radicals in the standard precursor.

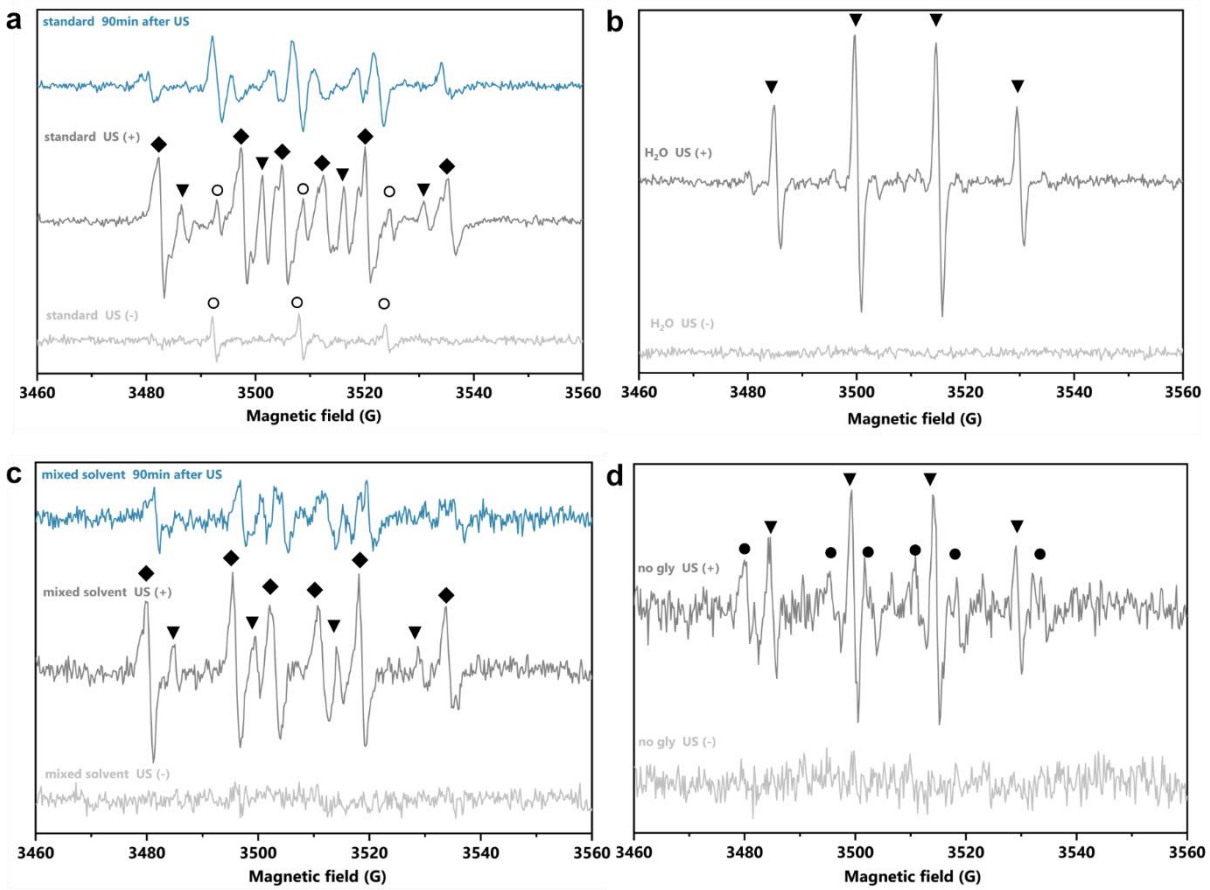

Figure 4.5 Mechanism study at the microscopic level by EPR tests. **(a)** The standard precursor **(b)** Water alone **(c)** The mixed solvent (water/glycerol 1:1, w/w) **(d)** The precursor without glycerol was measured before (light grey), right after (dark grey), or 90 minutes after 1-min sonication. DMPO = 2 mg/ml; US intensity 56 W cm^{-2}. ■ – DMPO•-R (hydroxyalkyl), α_N =

15.3G, α_H^β = 22.7G, g = 2.0088. ▼—DMPO•-OH, α_N = 14.8G, α_H^β = 14.8G, g = 2.0088. ●—DMPO•-R (alkyl), α_N = 15.5G, α_H^β = 22.8G, g = 2.0088.○—decomposition products of DMPO, α_N = 15.7G. The hyperfine coupling constants of α were obtained by fitting spectra using SpinFit.

Next, we studied the macroscopic gelation profiles of precursor solution with varying glycerol ratios (φ_g). (**Figure 4.6a**) It turned out that the required time to form a bulk gel was inversely relevant to φ_g. An extreme condition is without glycerol, no gels would form within the observation period (or the gelation time approaches infinity). When φ_g = 25 and 40 wt% respectively, it takes nearly 4 minutes and 3 minutes to complete the gelation transition, and a longer period is needed to reach the peak modulus. In comparison, we could expect to get sonogels within 2 minutes at the φ_g of 50 or 60 wt%, while even between these two groups, gels from the 60 wt% group reached the maximum modulus faster. Since acrylamide monomers and glycerol molecules can generate alkyl or hydroxyalkyl radicals respectively upon acoustic cavitation, both species are capable of initiating polymerization followed by gelation without external disruption. However, the participation of oxygen (due to either residual dissolving in solution or a non-strict closed reaction environment) changes the reaction pathway of the above two reactive species profoundly. (**Figure 4.6c**) Specifically, the conjugated effect of lone electron pairs of oxygen stabilizes the glycerol-cleaved hydroxyalkyl radicals to some degree, while the strong electron-withdrawing effect from the amide group makes its corresponding alkyl radicals at a higher energy state and thus easier to get oxidized by oxygen. Therefore, mere alkyl radicals could not initiate the gelation effectively in the glycerol-free system, and glycerol acts as the indispensable benign initiators in supporting sonogel formation. Besides, we compared the toughness of sonogels from each group, where all groups were sonicated for 4 minutes to ensure the gelation transformation finished. (**Figure 4.6b**) It turned out that the fracture energy declined with increasing glycerol amount in a monotonical modality. Given

that the contribution of the alginate network to the fracture energy of the hydrogel remains nearly constant, the observed differences in test results are primarily ascribed to variations in the density and properties of the load-bearing strands within the sono-polymerized PAAm network. From a qualitative view, a higher glycerol amount suggests a higher instant concentration of initiators, more chain-propagation sites, and thereby shorter segments on average between crosslinking points. Moreover, due to the dual functions of glycerol as benign initiators and viscosity modifiers in the solvent, a higher glycerol ratio possibly accompanies earlier chain termination or chain transfer to form large quantities of dangling chain-represented defects inside the network (**Supplementary Figure 4.14**), which also elucidates why the 60 wt% group has the lowest modulus.

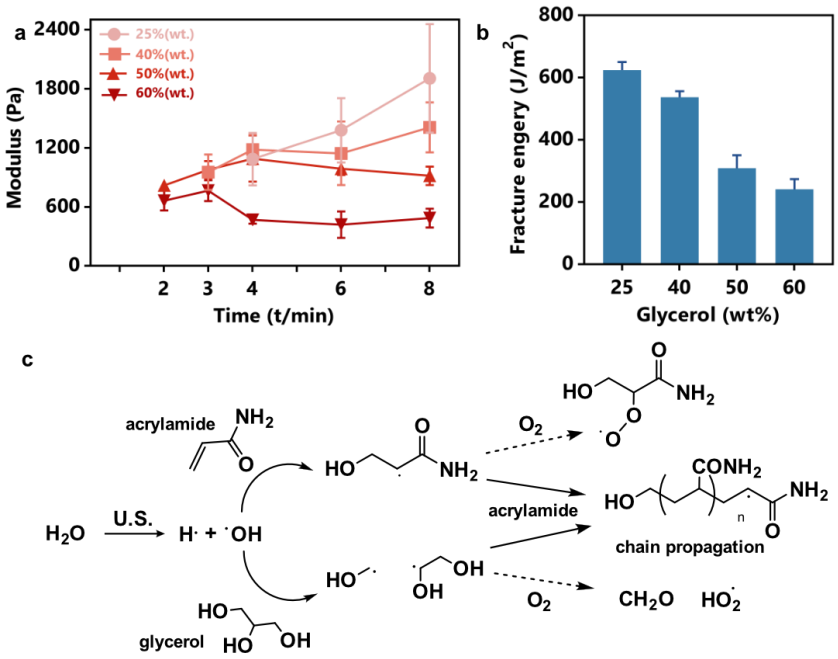

Figure 4.6 Kinetic study toward sonochemical gelation at the macroscopic level. **(a)** The gelation profiles and **(b)** The fracture energy of PAAm-alginate tough sonogels prepared at varying glycerol ratios. **(c)** Schematic of the proposed mechanism

In addition, glycerol affects the gelation profile by regulating the physical properties of liquid media as well, like viscosity and vapor pressure, which could play a synergistic role as its chemical function. For instance, a higher glycerol ratio results in increased solution viscosity and elevated vapor pressure. Although this raises the cavitation threshold, a more intense

condition of sonochemical reactions generated during bubble implosion would contribute to an enhancing initiation and gelation efficiency. (**Supplementary Figure 4.15**) Still, we believe the chemical role of glycerol is more determinative and substantial to the success of sonogel synthesis compared with its physical influences.

It should be noted that due to challenges including the establishment of an in situ EPR test platform for sono-synthesis and the intrinsic coupling of alkyl and hydroxyalkyl radicals, we could not explain the effect of glycerol ratios from molecular kinetics temporarily. Besides, the physical impact of glycerol also remains to be quantified. Nonetheless, the combined results at multiscale levels could still provide convincing proof to validate the above-proposed qualitative mechanisms, which could be further applied to targeted control of sonogel synthesis.

4.3. Synthesis-Property Relationship of Tough Sonogels

As a new methodology for tough gel preparation, the structure-property relationship of sonogels remains to be built. In this part, we first studied the effects of US intensity on gelation profile. As illustrated in **Figure 4.7a**, 32 W cm^{-2} was the lowest power density that supported the gelation, just above the cavitation threshold, and the transition needed at least 3 minutes. In comparison, we could expect to get a gel within 2 minutes when raising the intensity to 44 or 56 W cm^{-2}. A higher peak acoustic pressure facilitated more intense cavitation and liquid streaming, thereby creating more hot spots, and enhancing the diffusion of reactive species. However, further increasing the power would not accelerate that process but inversely require a longer period to form a gel, and the as-prepared gels also had a lower modulus. Moreover, sonogels prepared at 32 and 44 W cm^{-2} kept strengthening during the observed time range, while the other two groups reached their peak modulus earlier at 4 minutes. We attributed this nonlinear correspondence between the gelation time or the sonogel modulus and the sonication power to a continuing competition between constructive sonochemical reactions and

destructive mechanical disruptions.

Next, we investigated the influence of monomer-to-crosslinker ratios (**Figure 4.7b**), where the sonication time was fixed at 4 minutes and m_g was 40 wt%. Compared with thermal or photo-initiated hydrogels, there exists not only a much higher threshold of the required crosslinker amount to form sonogels but deeply coupled with US intensity. The recorded $\varphi_{m,min}$ was 1.69%, nearly two orders of magnitude higher than in common hydrogels. It's worth mentioning that this transition only happened at I = 32 W cm^{-2} while a higher sonication power led to failed gelation. We assumed the unusually high threshold and intrinsic coupling mechanism were due to liquid streaming, mixing, and shearing effects accompanied by cavitation. These dynamic mechanical perturbations lowered the utilization efficiency of crosslinking agents. Besides, the optimal φ_m at the maximum toughness showed a positive relevance to I, which increased from 14 (at 32 W cm^{-2}) to 19 (at 44 W cm^{-2}) and finally 29 (at 56 W cm^{-2}). At small I, more crosslinkers compensated for the less efficient gelation caused by insufficient initiation conditions, which primarily played a constructive role in 'forming a gel'. With I no longer a limited factor in the sonogel formation, extra crosslinking agents would lead to a denser PAAm network and shorter chain segments of load-bearing strands, macroscopically performing as a decreasing toughness with a lower φ_m.

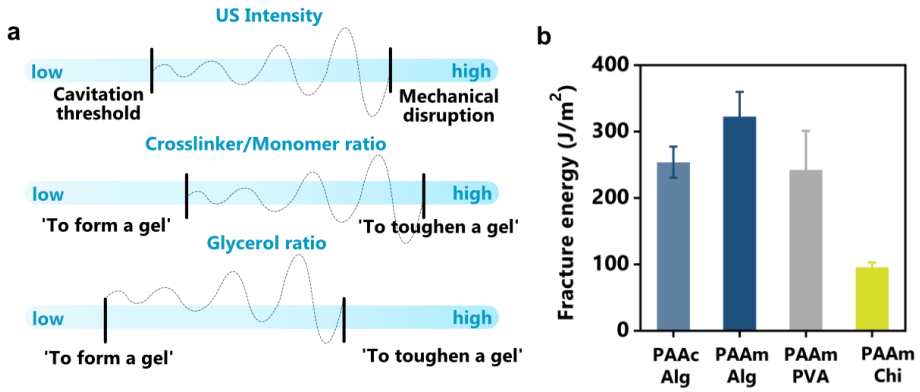

Figure 4.7 Benchmark the synthesis-property relationship of DN tough sonogels. **(a)** The qualitative gelation profiles of sonogels prepared under varying US intensities (from light to dark red, 32, 44, 56, and 68 W cm^{-2}). **(b)** The toughness of sonogels with different monomer-

to-crosslinker ratios and under various US intensities (from light to dark blue, 32, 44, and 56 W cm^{-2}).

So far, we have benchmarked the effects of various synthetic factors in two aspects, which could be straightforwardly summarized as forming a gel and toughening a gel (**Figure 4.8a**). To complete the gelation transformation, it requires I_{min} to surpass the cavitation threshold, $\varphi_{m,min}$ to offset the adverse effects of US, and certain φ_g to offer polyol radicals and increase systemic viscosity. However, all these variants are not separate and linearly correlated with the mechanical properties, in particular, toughness, of the resulting sonogels. They must be played around comprehensively and rationally in the preparation of tough sonogels.

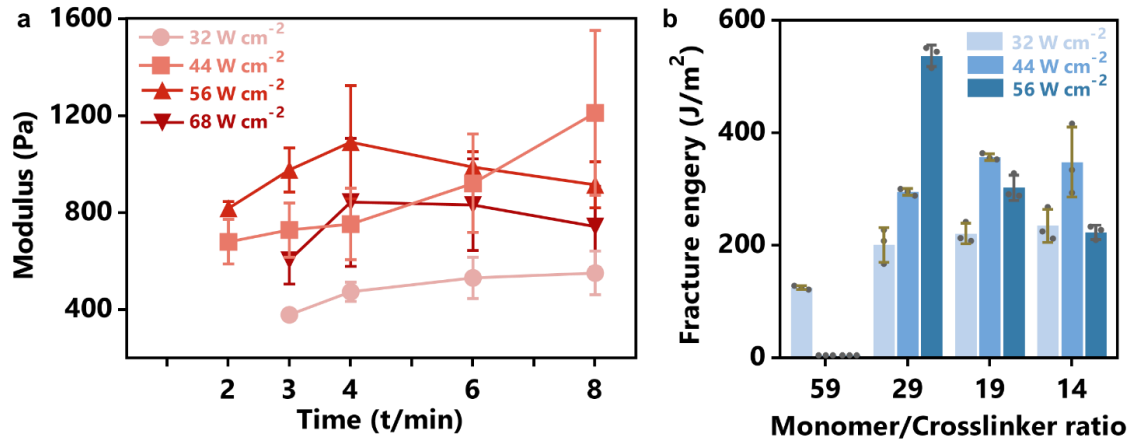

Figure 4.8 (a) Schematic showing the determinative synthetic factors to form a gel or to toughen a gel. **(b)** The fracture energy of various sonogels. (light blue, PAAc-alginate; dark blue, PAAm-alginate; light grey, PAAm-PVA; yellow green, PAAm-chitosan)

As a universal methodology, cavitation-driven sonogel synthesis applies to nearly all vinyl monomers, and so does the above-built synthesis-property relationship in terms of modification. We tried to construct multiple DN sonogels including the poly(acrylic acid) (PAAc)-alginate hydrogel, PAAm-poly(vinyl alcohol) (PVA) hydrogel, as well as PAAm-chitosan hydrogel, and they all showed comparable toughness. (**Figure 4.8b**) Finally, we horizontally compared the mechanical and structural characteristics of hydrogels prepared from conventional thermal or photo pathways and sonogels. It turned out that sonogels not only have a much faster gelation

transformation but perform more exceptional toughness over other groups. (**Figure 4.9a**) In particular, a substantial difference was distinguished between sonogels and thermal-initiated hydrogels in terms of gelation principles and kinetics. SEM images showed that sonogels had a uniform honeycomb-like microstructure with the highest porosity, while gels cured at room temperature had average larger but less uniform pores. The thermal-initiated gel illustrated a similar microstructure to sonogels but with a smaller pore size. On the other hand, the hydrogel solidified under UV irradiation seemed to possess the densest branch-like structure. We ascribed the structural specialty of sonogel to the broad seeding of cavitation bubbles during initiation and uniformly growing chains by sustained mechanical perturbation.

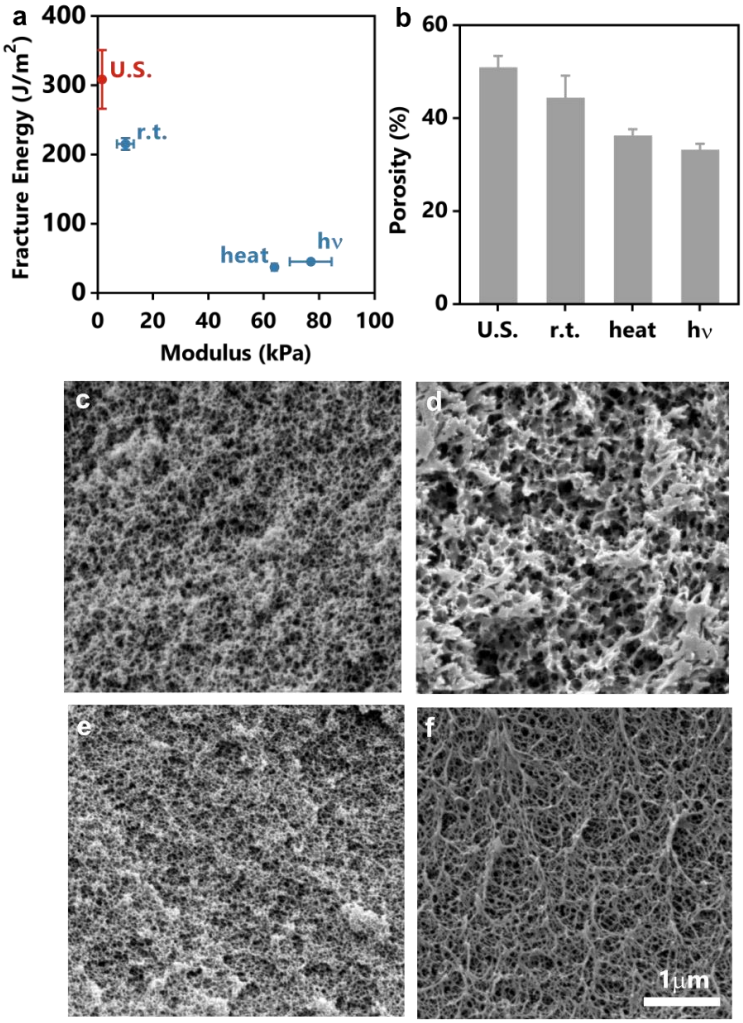

Figure 4.9 (a) The toughness-modulus graph and **(b)** The porosity of gels prepared under 20kHz ultrasound (no initiator, 56 W cm^{-2}, 4 minutes), room temperature (no initiator, 1 week),

heat (40°C oven, 0.5 wt% APS as initiators, 8 hours), and UV light (wavelength 365nm, 0.5 wt% α-keto glutaric acid as initiators, 1 hour). **(c-f)** SEM images of **(c)** sonogels **(d)** gels cured under room temperature **(e)** thermal-initiated gels **(f)** photo-initiated gels.

4.4. Supporting Information

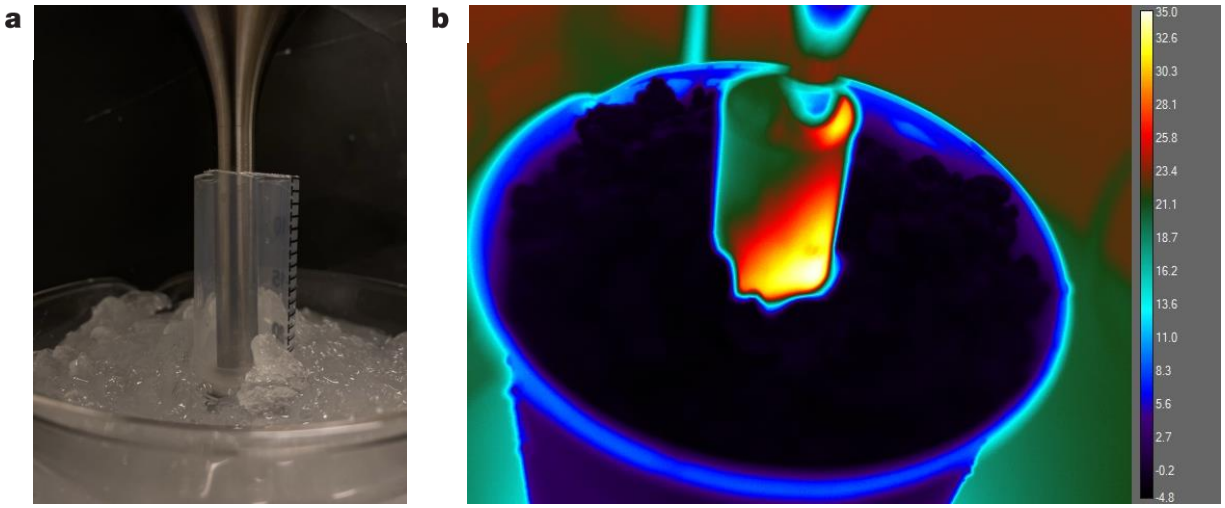

Figure 4.10 Exothermic characterization of the sonogel preparation process. (a) Experimental setup and (b) representative temperature profiles captured by an infrared thermal camera over time when ultrasound (56 W cm-2) is applied in the precursor solution.

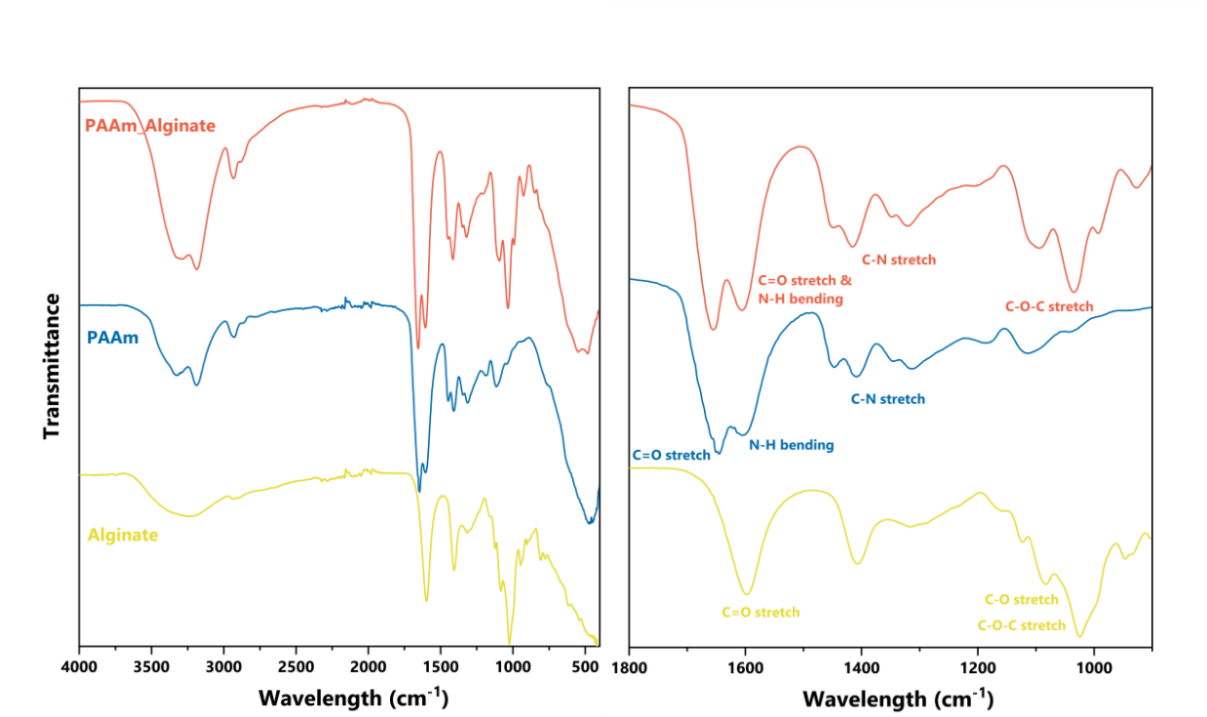

Figure 4.11 FTIR spectra of the prepared PAAm-alginate sonogel as well as commercially available PAAm and alginate samples. The spectrum of DN sonogel has characteristic signal peaks of both PAAm and alginate, suggesting successful polymerization and crosslinking of the two networks.

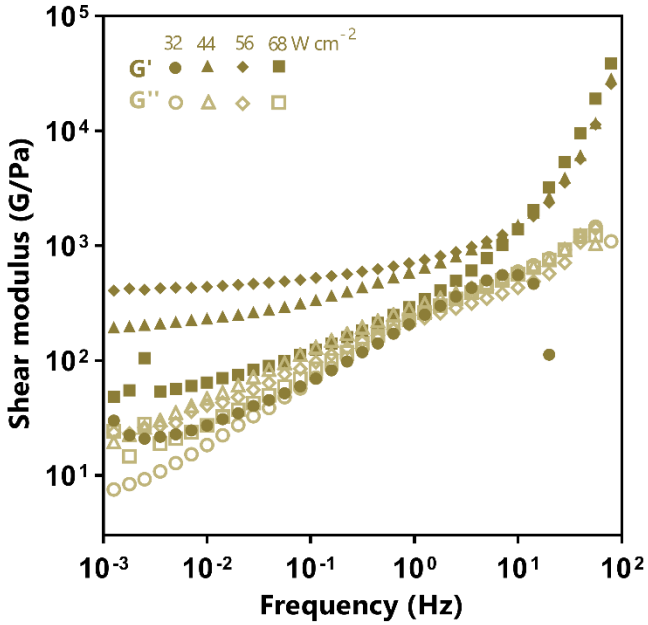

Figure 4.12 Frequency sweep to measure the storage and loss modulus of sonogels prepared under different ultrasound intensities (dark filled symbols, storage modulus G′; light unfilled symbols, loss modulus G″; circular symbols, 32 W cm^{-2}; triangular symbols, 44 W cm^{-2}; diamond symbols, 56 W cm^{-2}; rectangular symbols: 68 W cm^{-2}.

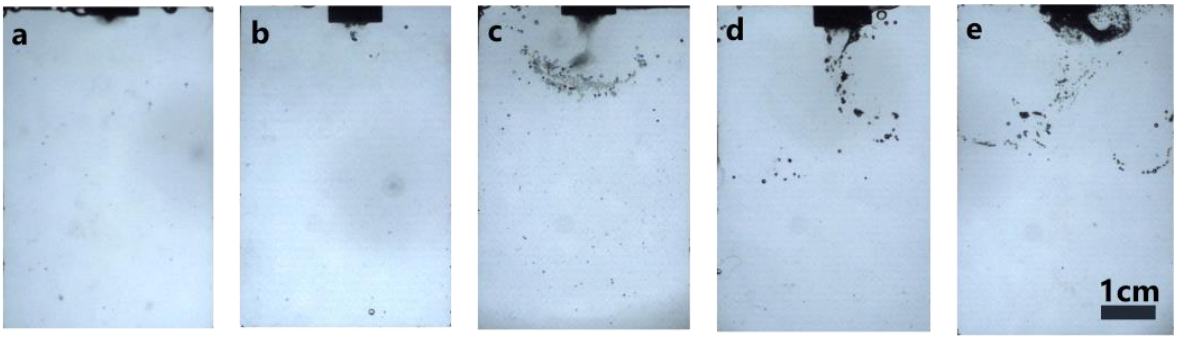

Figure 4.13 High-speed imaging of sonogels prepared under different US intensities. Screenshots were taken 6 min after sonication started. (from a to e, 24, 32, 44, 56, 68 W cm^{-2} respectively)

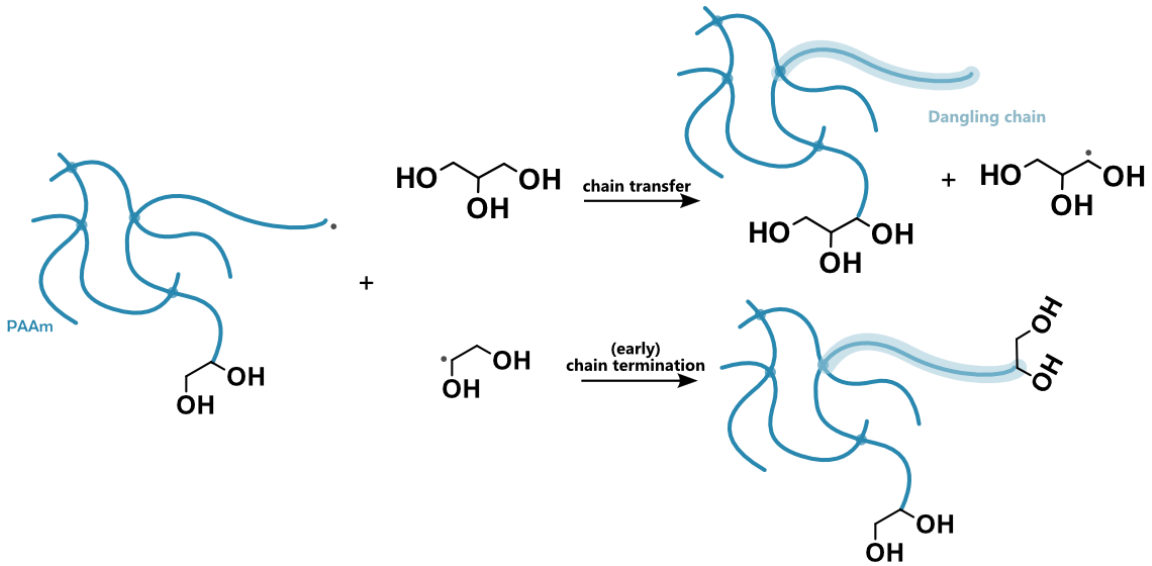

Figure 4.14 Schematic of proposed mechanism about the effect of glycerol ratios on sonogel toughness. As glycerol plays two-fold functions as initiator supplier and solvent, the possibility of chain transfer or early chain termination would also increase with a higher glycerol ratio in the mixture, leading to an overall lower fracture energy of the resulting gels.

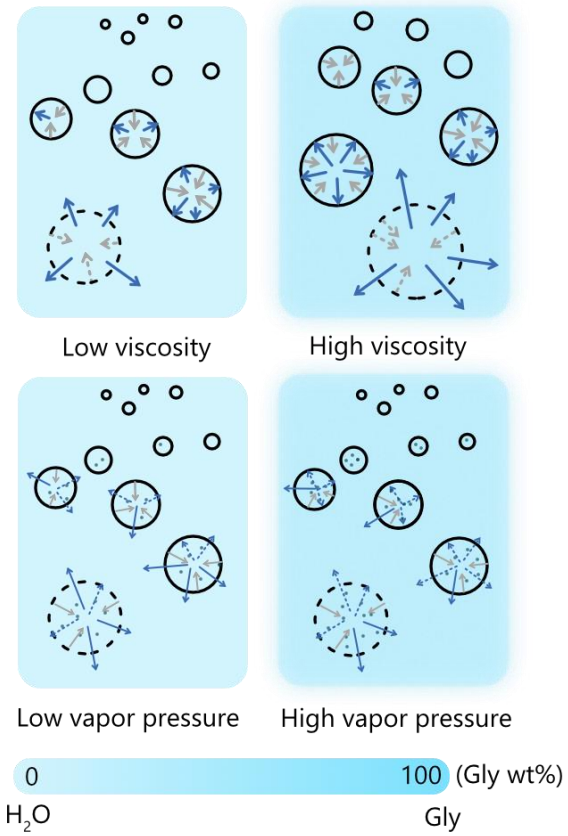

Figure 4.15 Schematic of proposed mechanism about the effect of glycerol ratios on the sono-initiation process. **(a)** The higher the glycerol ratio, the higher the viscosity and the more intense the localized conditions generated by collapsing bubbles. **(b)** A higher glycerol amount

also raises the vapor pressure of the mixture, weakening the cushion effect induced by vapor voids and maintaining a harsh condition of imploded bubbles.

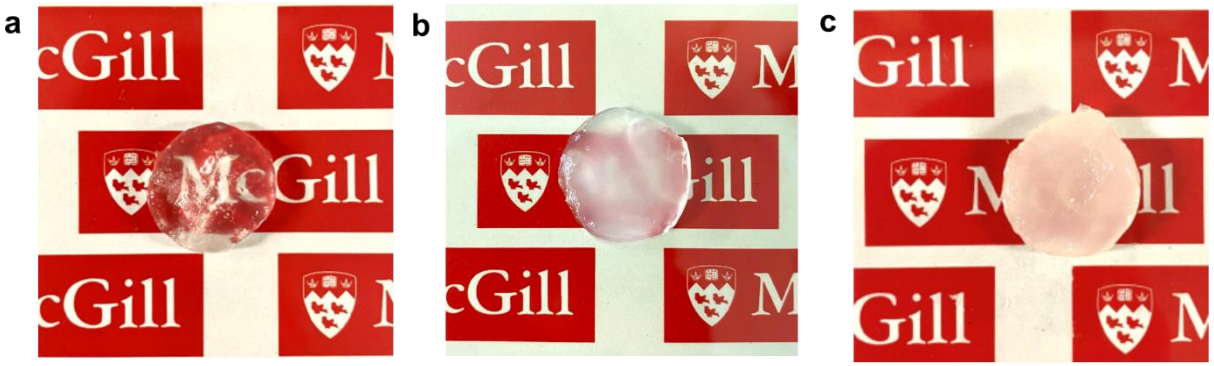

Figure 4.16 Digital images of diverse sono-synthesized DN hydrogels. **(a)** PAAc-alginate **(b)** PAAm-PVA **(c)** PAAm-chitosan.

Chapter 5. Conclusion and Outlook

5.1. Conclusion

In this thesis, we established the synthesis-property relationship of DN tough sonogels through EPR study and mechanical characterization, aiming to provide a fundamental perspective on the application of mechano- or sonochemistry in hydrogel preparation and relevant soft matter engineering.

In the first part, the new paradigm of tough sonogel preparation has been formulated. High-speed and polarized imaging reveals the dynamic impact of cavitation-induced mechanochemistry on the process of gelation transformation. The broadly seeded cavitation bubbles constitute an initiating network to facilitate concurrent propagation and rapid crosslink of polymer chains at multiple points. By tracking its motion under polarized filters, we could intuitively anticipate the approximate gelation area. For another, strong shearing would dampen load-bearing strands and cause defects in the as-formed bulk gel. In correspondence, a peak modulus is observed in the gelation profile. Through post-crosslinking in $CaCl_2$ solution, the hybrid DN gel showed an average fracture energy of around 300 J m^{-2}.

Subsequently, we discovered the underlying sonochemical mechanism by synergistic multiscale study. On the one hand, EPR results showed that both acrylamide monomers and solvent molecules (either water or glycerol) could generate active species upon sonication to further launch the reaction. However, the relative instability of acrylamide alkyl radicals makes it challenging to fulfill effective chain propagation with the involvement of oxygen. In comparison, hydroxyalkyl radicals from glycerol act as benign initiators and enable the completion of sonogel formation even in an air-exposure environment. Macroscopic gelation profiles also validated this hypothesis that a higher glycerol ratio in the mixture would shorten the time period of gel transition. The introduction of glycerol as part of the solvent is also

beneficial for enhancing system viscosity and vapor pressure, further accelerating the progress of the reaction.

Furthermore, we quantified the influence of other determinative parameters on the mechanical properties of sonogels, including ultrasound intensity and monomer-to-crosslinker ratio. By playing around these factors comprehensively, we can orientally synthesize or toughen sonogels. SEM images revealed the microstructural specialty of sonogels, including a comparatively high porosity and uniformity. Differing from mild thermal or photo-initiation, powerful agitation and streaming yielded from cavitation reduce the utilization of crosslink agents and endow the resulting gel with an overall better performance in toughness.

5.2. Outlook

Based on the above essential understanding, more research intersecting hydrogels and ultrasound can be advanced either in fundamental sonochemistry or engineering applications. We listed several challenges and opportunities in the following.

In the scientific realm, limited by challenges in carrying out in-situ EPR measurements during sono-gelation, we are provisionally unable to quantitatively reveal the polymerization kinetics at the molecular level. Cascade and competitive reactions between active free-radical species exacerbate that difficulty. For instance, the homolytic cleaved alkyl or hydroxyalkyl radicals would possibly get oxidized, captured by spin traps, or continue to initiate the polymerization. Moreover, glycerol undertakes two-fold roles in facilitating sono-gelation and participates in multiple reaction steps, making it hard to give a numerical interpretation toward a separate aspect, for instance, its regulation with physical properties of the mixture. Acoustic simulation and theoretical models could help monitor mechanical effects and estimate its influence during sono-gelation.

For engineering, the establishment of synthesis-property relationship paves the way for

advanced manufacturing and application of sonogels as well. As introduced in section 2.2.3, PEGDA-based sono inks have been developed recently supporting acoustic volumetric printing. However, the driving force of its gelation is the rising temperature induced by sonothermal effects, which is substantially distinct from acoustic cavitation that we investigated here. Thermal initiators are still necessary to fulfill instant solidification in that case. According to the aforementioned sonochemical mechanism, we wonder whether a cavitation-activated sono-printing platform could be created to allow initiator-free sonogel fabrication for both small-molecule or oligo vinyl monomers. This anticipates to further eliminate the negative impacts of residual initiators, particularly in the bioprinting setting.

References

1. X. Zhao, Multi-scale multi-mechanism design of tough hydrogels: building dissipation into stretchy networks. *Soft Matter* **10**, 672-687 (2014).
2. J.-Y. Sun *et al.*, Highly stretchable and tough hydrogels. *Nature* **489**, 133-136 (2012).
3. J. P. Gong, Materials both Tough and Soft. *Science* **344**, 161-162 (2014).
4. J. P. Gong, Y. Katsuyama, T. Kurokawa, Y. Osada, Double-network hydrogels with extremely high mechanical strength. *Advanced materials* **15**, 1155-1158 (2003).
5. J. P. Gong, Why are double network hydrogels so tough? *Soft Matter* **6**, 2583-2590 (2010).
6. T. Dai, X. Qing, Y. Lu, Y. Xia, Conducting hydrogels with enhanced mechanical strength. *Polymer* **50**, 5236-5241 (2009).
7. Hierarchically Designed Agarose and Poly(Ethylene Glycol) Interpenetrating Network Hydrogels for Cartilage Tissue Engineering. *Tissue Engineering Part C: Methods* **16**, 1533-1542 (2010).
8. F. Luo *et al.*, Oppositely charged polyelectrolytes form tough, self-healing, and rebuildable hydrogels. *Adv Mater* **27**, 2722-2727 (2015).
9. H. Fan *et al.*, Adjacent cationic-aromatic sequences yield strong electrostatic adhesion of hydrogels in seawater. *Nat Commun* **10**, 5127 (2019).
10. T. L. Sun *et al.*, Physical hydrogels composed of polyampholytes demonstrate high toughness and viscoelasticity. *Nat Mater* **12**, 932-937 (2013).
11. W. R. Illeperuma, J.-Y. Sun, Z. Suo, J. J. Vlassak, Fiber-reinforced tough hydrogels. *Extreme Mechanics Letters* **1**, 90-96 (2014).
12. T. Matsuda, R. Kawakami, R. Namba, T. Nakajima, J. P. Gong, Mechanoresponsive self-growing hydrogels inspired by muscle training. *Science* **363**, 504-508 (2019).
13. Z. J. Wang *et al.*, Azo-Crosslinked Double-Network Hydrogels Enabling Highly Efficient Mechanoradical Generation. *J Am Chem Soc* **144**, 3154-3161 (2022).
14. S. Y. Zheng *et al.*, Slide-ring cross-links mediated tough metallosupramolecular hydrogels with superior self-recoverability. *Macromolecules* **52**, 6748-6755 (2019).
15. T. Sakai *et al.*, Highly Elastic and Deformable Hydrogel Formed from Tetra-arm Polymers. *Macromolecular Rapid Communications* **31**, 1954-1959 (2010).
16. S. Fuchs, K. Shariati, M. Ma, Specialty Tough Hydrogels and Their Biomedical Applications. *Advanced Healthcare Materials* **9**, 1901396 (2020).
17. M. Hua *et al.*, Strong tough hydrogels via the synergy of freeze-casting and salting out. *Nature* **590**, 594-599 (2021).
18. Y. Okumura, K. Ito, The polyrotaxane gel: A topological gel by figure-of-eight cross-links. *Advanced materials* **13**, 485-487 (2001).
19. K. Ito, Novel cross-linking concept of polymer network: synthesis, structure, and properties of slide-ring gels with freely movable junctions. *Polymer journal* **39**, 489-499 (2007).
20. A. Bin Imran *et al.*, Extremely stretchable thermosensitive hydrogels by introducing slide-ring polyrotaxane cross-linkers and ionic groups into the polymer network. *Nature communications* **5**, 5124 (2014).

21. C. Liu, H. Kadono, H. Yokoyama, K. Mayumi, K. Ito, Crack propagation resistance of slide-ring gels. *Polymer* **181**, 121782 (2019).
22. C. Liu *et al.*, Tough hydrogels with rapid self-reinforcement. *Science* **372**, 1078-1081 (2021).
23. G. Nian, J. Kim, X. Bao, Z. Suo, Making Highly Elastic and Tough Hydrogels from Doughs. *Adv Mater*, e2206577 (2022).
24. X. D. Feng, X. Q. Guo, K. Y. Qiu, Study of the initiation mechanism of the vinyl polymerization with the system persulfate/N, N, N′, N′-tetramethylethylenediamine. *Die Makromolekulare Chemie: Macromolecular Chemistry and Physics* **189**, 77-83 (1988).
25. M. Shirangi *et al.*, Methyleneation of Peptides by N,N,N,N-Tetramethylethylenediamine (TEMED) under Conditions Used for Free Radical Polymerization: A Mechanistic Study. *Bioconjugate Chemistry* **26**, 90-100 (2015).
26. Y. Yagci, S. Jockusch, N. J. Turro, Photoinitiated Polymerization: Advances, Challenges, and Opportunities. *Macromolecules* **43**, 6245-6260 (2010).
27. R. L. Truby, J. A. Lewis, Printing soft matter in three dimensions. *Nature* **540**, 371-378 (2016).
28. Z. Chen *et al.*, 3D printing of multifunctional hydrogels. *Advanced Functional Materials* **29**, 1900971 (2019).
29. J. Li, C. Wu, P. K. Chu, M. Gelinsky, 3D printing of hydrogels: Rational design strategies and emerging biomedical applications. *Materials Science and Engineering: R: Reports* **140**, 100543 (2020).
30. S. Dutta, D. Cohn, Temperature and pH responsive 3D printed scaffolds. *Journal of Materials Chemistry B* **5**, 9514-9521 (2017).
31. D. Han, Z. Lu, S. A. Chester, H. Lee, Micro 3D printing of a temperature-responsive hydrogel using projection micro-stereolithography. *Scientific reports* **8**, 1963 (2018).
32. X. Kuang, M. O. Arıcan, T. Zhou, X. Zhao, Y. S. Zhang, Functional Tough Hydrogels: Design, Processing, and Biomedical Applications. *Accounts of Materials Research* **4**, 101-114 (2023).
33. J. Li *et al.*, Tough adhesives for diverse wet surfaces. *Science* **357**, 378-381 (2017).
34. S. J. Wu, X. Zhao, Bioadhesive Technology Platforms. *Chemical Reviews* **123**, 14084-14118 (2023).
35. J. Yang, R. Bai, B. Chen, Z. Suo, Hydrogel Adhesion: A Supramolecular Synergy of Chemistry, Topology, and Mechanics. *Advanced Functional Materials* **30**, (2019).
36. Z. Ma, G. Bao, J. Li, Multifaceted Design and Emerging Applications of Tissue Adhesives. *Advanced Materials* **33**, 2007663 (2021).
37. H. Yuk *et al.*, Dry double-sided tape for adhesion of wet tissues and devices. *Nature* **575**, 169-174 (2019).
38. X. Chen, H. Yuk, J. Wu, C. S. Nabzdyk, X. Zhao, Instant tough bioadhesive with triggerable benign detachment. *Proc Natl Acad Sci U S A* **117**, 15497-15503 (2020).
39. J. Deng *et al.*, Electrical bioadhesive interface for bioelectronics. *Nat Mater* **20**, 229-236 (2021).
40. K. Arakaki *et al.*, Artificial cartilage made from a novel double-network hydrogel: In

vivo effects on the normal cartilage and ex vivo evaluation of the friction property. *Journal of Biomedical Materials Research Part A* **93A**, 1160-1168 (2010).
41. D. Wang *et al.*, Microfluidic bioprinting of tough hydrogel-based vascular conduits for functional blood vessels. *Science Advances* **8**, eabq6900 (2022).
42. Z. Luo *et al.*, Vertical Extrusion Cryo(bio)printing for Anisotropic Tissue Manufacturing. *Advanced Materials* **34**, 2108931 (2022).
43. Y. Lee, W. J. Song, J. Y. Sun, Hydrogel soft robotics. *Materials Today Physics* **15**, 100258 (2020).
44. Y. Kim, X. Zhao, Magnetic soft materials and robots. *Chemical reviews* **122**, 5317-5364 (2022).
45. W. J. Zheng, N. An, J. H. Yang, J. Zhou, Y. M. Chen, Tough Al-alginate/poly (N-isopropylacrylamide) hydrogel with tunable LCST for soft robotics. *ACS applied materials & interfaces* **7**, 1758-1764 (2015).
46. H. Yuk *et al.*, Hydraulic hydrogel actuators and robots optically and sonically camouflaged in water. *Nature communications* **8**, 14230 (2017).
47. K. S. Suslick, Sonochemistry. *science* **247**, 1439-1445 (1990).
48. D. Dalecki, D. C. Hocking, Ultrasound technologies for biomaterials fabrication and imaging. *Ann Biomed Eng* **43**, 747-761 (2015).
49. A. Azagury, L. Khoury, G. Enden, J. Kost, Ultrasound mediated transdermal drug delivery. *Adv Drug Deliv Rev* **72**, 127-143 (2014).
50. K. S. Suslick, The chemical effects of ultrasound. *Scientific American* **260**, 80-87 (1989).
51. K. S. Suslick, Mechanochemistry and sonochemistry: concluding remarks. *Faraday discussions* **170**, 411-422 (2014).
52. T. G. McKenzie, F. Karimi, M. Ashokkumar, G. G. Qiao, Ultrasound and Sonochemistry for Radical Polymerization: Sound Synthesis. *Chemistry* **25**, 5372-5388 (2019).
53. Y. T. Didenko, W. B. McNamara, K. S. Suslick, Hot spot conditions during cavitation in water. *Journal of the American Chemical Society* **121**, 5817-5818 (1999).
54. D. J. Flannigan, S. D. Hopkins, C. G. Camara, S. J. Putterman, K. S. Suslick, Measurement of pressure and density inside a single sonoluminescing bubble. *Phys Rev Lett* **96**, 204301 (2006).
55. K. S. Suslick, N. C. Eddingsaas, D. J. Flannigan, S. D. Hopkins, H. Xu, Extreme conditions during multibubble cavitation: Sonoluminescence as a spectroscopic probe. *Ultrason Sonochem* **18**, 842-846 (2011).
56. K. S. Suslick, D. J. Flannigan, Inside a collapsing bubble: sonoluminescence and the conditions during cavitation. *Annu Rev Phys Chem* **59**, 659-683 (2008).
57. P. Kanthale, M. Ashokkumar, F. Grieser, Sonoluminescence, sonochemistry (H2O2 yield) and bubble dynamics: Frequency and power effects. *Ultrasonics Sonochemistry* **15**, 143-150 (2008).
58. M. M. Caruso *et al.*, Mechanically-induced chemical changes in polymeric materials. *Chemical reviews* **109**, 5755-5798 (2009).
59. in *Applied Sonochemistry*. (2002), pp. 75-130.

60. K. S. Suslick, G. J. Price, APPLICATIONS OF ULTRASOUND TO MATERIALS CHEMISTRY. *Annual Review of Materials Science* **29**, 295-326 (1999).
61. J. H. Bang, K. S. Suslick, Applications of ultrasound to the synthesis of nanostructured materials. *Adv Mater* **22**, 1039-1059 (2010).
62. J. M. J. Paulusse, R. P. Sijbesma, Ultrasound in polymer chemistry: Revival of an established technique. *Journal of Polymer Science Part A: Polymer Chemistry* **44**, 5445-5453 (2006).
63. A. H. Lebovitz, M. K. Gray, A. C. Chen, J. M. Torkelson, Interpolymer radical coupling reactions during sonication of polymer solutions. *Polymer* **44**, 2823-2828 (2003).
64. G. J. Price, P. F. Smith, P. J. West, Ultrasonically initiated polymerization of methyl methacrylate. *Ultrasonics* **29**, 166-170 (1991).
65. G. J. Price, E. J. Lenz, The use of dosimeters to measure radical production in aqueous sonochemical systems. *Ultrasonics* **31**, 451-456 (1993).
66. D. J. Donaldson, M. D. Farrington, P. Kruus, Cavitation-induced polymerization of nitrobenzene. *Journal of Physical Chemistry* **83**, 3130-3135 (1979).
67. S. Kanmuri, V. S. Moholkar, Mechanistic aspects of sonochemical copolymerization of butyl acrylate and methyl methacrylate. *Polymer* **51**, 3249-3261 (2010).
68. V. Selvaraj, P. Sakthivel, V. Rajendran, Effect of ultrasound in the free radical polymerization of acrylonitrile under a new multi-site phase-transfer catalyst–A kinetic study. *Ultrasonics sonochemistry* **22**, 265-271 (2015).
69. T. G. McKenzie *et al.*, Beyond Traditional RAFT: Alternative Activation of Thiocarbonylthio Compounds for Controlled Polymerization. *Advanced Science* **3**, 1500394 (2016).
70. Z. Wang *et al.*, Ultrasonication-Induced Aqueous Atom Transfer Radical Polymerization. *ACS Macro Letters* **7**, 275-280 (2018).
71. K. Sankar, V. Rajendran, Polymerization of ethyl methacrylate under the influence of ultrasound assisted a new multi-site phase-transfer catalyst system–A kinetic study. *Ultrasonics sonochemistry* **20**, 329-337 (2013).
72. B. Rokita, J. M. Rosiak, P. Ulanski, Ultrasound-Induced Cross-Linking and Formation of Macroscopic Covalent Hydrogels in Aqueous Polymer and Monomer Solutions. *Macromolecules* **42**, 3269-3274 (2009).
73. P. Cass, W. Knower, E. Pereeia, N. P. Holmes, T. Hughes, Preparation of hydrogels via ultrasonic polymerization. *Ultrason Sonochem* **17**, 326-332 (2010).
74. S. R. Yang, Y. Y. Yeh, Y. C. Yeh, Ultrasound-triggered hydrogel formation through thiol-norbornene reactions. *Chem Commun (Camb)* **58**, 1119-1122 (2022).
75. Z. Ma *et al.*, Controlled tough bioadhesion mediated by ultrasound. *Science* **377**, 751-755 (2022).
76. M. Habibi, S. Foroughi, V. Karamzadeh, M. Packirisamy, Direct sound printing. *Nat Commun* **13**, 1800 (2022).
77. X. Kuang *et al.*, Self-enhancing sono-inks enable deep-penetration acoustic volumetric printing. *Science* **382**, 1148-1155 (2023).
78. Z. Wei, F. A. Villamena, L. K. Weavers, Kinetics and Mechanism of Ultrasonic Activation of Persulfate: An in Situ EPR Spin Trapping Study. *Environ Sci Technol* **51**,

3410-3417 (2017).
79. H. Laajimi, M. Mattia, R. S. Stein, C. L. Bianchi, D. C. Boffito, Electron paramagnetic resonance of sonicated powder suspensions in organic solvents. *Ultrason Sonochem* **73**, 105544 (2021).
80. H. Taniguchi, K. P. Madden, DMPO-alkyl radical spin trapping: an in situ radiolysis steady-state ESR study. *Radiation research* **153**, 447-453 (2000).
81. E. Finkelstein, G. M. Rosen, E. J. Rauckman, Spin trapping of superoxide and hydroxyl radical: practical aspects. *Archives of biochemistry and biophysics* **200**, 1-16 (1980).
82. A. Samuni, C. M. Krishna, P. Riesz, E. Finkelstein, A. Russo, Superoxide reaction with nitroxide spin-adducts. *Free Radical Biology and Medicine* **6**, 141-148 (1989).
83. J.-L. Clément *et al.*, Assignment of the EPR Spectrum of 5,5-Dimethyl-1-pyrroline N-Oxide (DMPO) Superoxide Spin Adduct. *The Journal of Organic Chemistry* **70**, 1198-1203 (2005).